

THE L – σ RELATION OF LOCAL H II GALAXIES

V. BORDALO AND E. TELLES

Observatório Nacional, Rua Gal. José Cristino, 77, CEP 20912-400, São Cristóvão, Rio de Janeiro, Brazil; vschmidt@on.br, etelles@on.br

Received 2010 September 3; accepted 2011 April 25; published 2011 June 15

ABSTRACT

For the first time we present a new data set of emission line widths for 118 star-forming regions in H II galaxies (HIIGs). This homogeneous set is used to investigate the L – σ relation in conjunction with optical spectrophotometric observations. We were able to classify their nebular emission line profiles due to our high-resolution spectra. Peculiarities in the line profiles such as sharp lines, wings, asymmetries, and in some cases more than one component in emission were verified. From a new independent homogeneous set of spectrophotometric data, we derived physical condition parameters and performed statistical principal component analysis. We have investigated the potential role of metallicity (O/H), H β equivalent width ($W_{H\beta}$), and ionization ratio [O III]/[O II] to account for the observational scatter of the L – σ relation. Our results indicate that the L – σ relation for HIIGs is more sensitive to the evolution of the current starburst event (short-term evolution) and dated by $W_{H\beta}$ or even the [O III]/[O II] ratio. The long-term evolution measured by O/H also plays a potential role in determining the luminosity of the current burst for a given velocity dispersion and age as previously suggested. Additionally, galaxies showing Gaussian line profiles present tighter correlations indicating that they are the best targets for the application of the parametric relations as an extragalactic cosmological distance indicator. Best fits for a restricted homogeneous sample of 45 HIIGs provide us with a set of new extragalactic distance indicators with an rms scatter compatible with observational errors of $\delta \log L_{H\alpha} = 0.2$ dex or 0.5 mag. Improvements may still come from future optimized observational programs to reduce the observational uncertainties on the predicted luminosities of HIIGs in order to achieve the precision required for the application of these relations as tests of cosmological models.

Key words: distance scale – galaxies: dwarf – galaxies: kinematics and dynamics – galaxies: starburst – H II regions

Online-only material: color figures

1. INTRODUCTION

Giant H II regions (GHIIRs) and H II galaxies (HIIGs) have been intensively studied for almost 40 years not only because they are natural laboratories for testing astrophysical models (Stasińska & Izotov 2003, and references therein) but also because they present tight scaling relations that can be useful as extragalactic distance estimators (Melnick et al. 2000; Melnick 2003; Siegel et al. 2005; Plionis et al. 2009).

The correlations between nebular diameter, luminosity (L), and velocity dispersion (σ) of the ionized gas in GHIIRs were found by Melnick (1977, 1978, 1979) and further investigated by Terlevich & Melnick (1981). Several other works from independent groups have confirmed the existence of these relations for GHIIRs in the Local Group’s Magellanic irregular galaxies and in some nearby spirals but there is no agreement about the calibration coefficients (slope and zero point), mainly due to different sample selections, observational data quality, and linear fit algorithms (Hippelein 1986; Melnick et al. 1987; Arsenault & Roy 1988; Fuentes-Masip et al. 2000; Bosch et al. 2002; Rozas et al. 2006). For HIIGs, these studies are more scarce. The first L – σ calibration was obtained by Melnick et al. (1988, hereafter MTM) with an rms scatter of $\delta \log L_{H\beta} \sim 0.30$, which is a landmark for follow-up achievements. In fact, part of this observed scatter has been proposed to be associated with a second parameter, namely oxygen abundance (MTM) or core radius (Telles & Terlevich 1993).

Despite the fact that the physical origin of the observed supersonic line widths has been a topic of intense debate in the literature, with no consensus (Terlevich & Melnick 1981; Tenorio-Tagle et al. 1993, 2006; Chu & Kennicutt 1994; Scalo

& Chappell 1999; Melnick et al. 1999; Bordalo et al. 2009), the L – σ relation remains as a potentially powerful alternative empirical extragalactic distance estimator to the classic Tully–Fisher for spirals and D_n – σ relations for ellipticals. This is still more exciting since Tully–Fisher and D_n – σ relations can only be applied up to redshift ~ 1 , where the relation is less affected by natural galaxy evolution with look-back time (Fernández Lorenzo et al. 2011, 2010). On the other hand, light curves of Type Ia supernovae (SNIa), which are today the most used technique to obtain such cosmological distances, encounter a lack of target objects at redshifts above ~ 1.2 (Riess et al. 2007).

There are, therefore, two possible roles for the L – σ relation: (1) to obtain distances to nearby galaxies, mainly in the Local Group where peculiar velocities are significant compared to cosmological recession velocities, and distances to nearby galaxy clusters where HIIGs can be found in the neighborhood and (2) to obtain distances to intermediate- and high-redshift galaxies (cosmological distances) to probe the dark energy equation of state parameter through Hubble diagram analysis. Several issues, however, should be further investigated for this latter goal with precision required in the era of “concordance cosmology”. (1) The origin of σ : the physical mechanism that produces the observed supersonic motions in the interstellar medium (ISM; e.g., gravity, turbulence, feedback, stochastic effects of the ISM, etc.). (2) The validity of the relation to high redshifts: the identification of bona fide HIIGs at great distances due to conspicuous emission lines should allow the validity test to be performed once a homogeneous set of kinematic and spectrophotometric data is gathered. (3) Systematic effects: evolutionary and other effects may affect the relation and may be parameterized (e.g., age of the starburst, metallicity, etc.).

(4) Observational errors: spectrophotometric calibration, distance, line width, and errors may still be suppressed so that the calibration can be competitive with other distance indicators of cosmological interest and so that the intrinsic scatter in the relation can be assessed. (5) Zero-point calibration: further improvement of the zero point for HII Gs may be achieved by a revision of the distances for GHII Rs in view of modern observations, and at the same time, the hypothesis that both classes follow the same relation as proposed by MTM can be tested.

Several recent works have investigated the kinematics of star-forming galaxies at high redshifts ($z \sim 2-3$; Law et al. 2009; Erb et al. 2004; Pettini et al. 2001). These studies have shown that most of the galaxies found exhibit high local velocity dispersions $\sim 60-100 \text{ km s}^{-1}$, suggesting that even for those galaxies with clear velocity gradients, rotation about a preferred kinematic axis may not be the dominant means of physical support. This has also been confirmed in local HII Gs (Moiseev et al. 2010; Bordalo et al. 2009; Martínez-Delgado et al. 2007; Maíz-Apellániz et al. 1999). Despite the fact that most of these distant galaxies have suffered a more violent and probably continuous star formation, which led them to become the normal galaxies found in the local universe, many of their juvenile physical properties are very similar to those found in local HII Gs. Therefore, these provide us with empirical support to speculate about the ambitious goal for using the $L-\sigma$ relation to determine distances of high-redshift galaxies.

In this paper, for the first time we present a large homogeneous data set of emission line width measurements of over 100 local HII Gs ($z < 0.1$), doubling the sample of MTM with velocity widths obtained from high-resolution spectra. These were combined with a complete set of spectrophotometric data obtained mostly from Kehrig et al. (2004, hereafter KTC) to produce a new calibration for the $L-\sigma$ relation. We investigated the potential role of different systematic effects over the $L-\sigma$ relation, such as age, metallicity, aperture, and non-Gaussianity of the emission line profiles. We argue that the detailed study of these effects is crucial for identifying a homogeneous sample for which the relation is valid and shedding light on its physical interpretation.

The paper is organized as follows. Section 2 describes the data, observations, and reductions. The results are presented in Section 3. In Section 4, we present our data analysis. We present a discussion about our results in Section 5 and summarize the conclusions in Section 6. The Hubble constant adopted throughout this work is $H_0 = 71 \text{ km s}^{-1} \text{ Mpc}^{-1}$.

2. DATA SAMPLE, OBSERVATIONS, AND REDUCTIONS

2.1. The Sample

We have selected most objects from the Spectrophotometric Catalogue of HII Galaxies (SCHGs; Terlevich et al. 1991, hereafter T91). It contains many galaxies from the Curtis Schmidt-Thin Prism Survey of Tololo (Tol; Smith et al. 1976) and the University of Michigan Survey (UM; MacAlpine et al. 1977). The SCHG also contains a few galaxies from the Fairall, Markarian, and Zwicky lists (Fairall 1980; Markarian 1967; Zwicky et al. 1966; hereafter F80, MRK, Zw, respectively). We have also selected HII Gs from smaller surveys such as those produced by Kunth et al. (1981, POX), Maza et al. (1991, CTS), and Surace & Comte (1998, hereafter SC98). Cambridge UK Schmidt galaxies (Cam) have been selected from Campbell et al. (1986). Note that some of the HII Gs were cataloged in more than one of these lists. Additionally, we have selected some

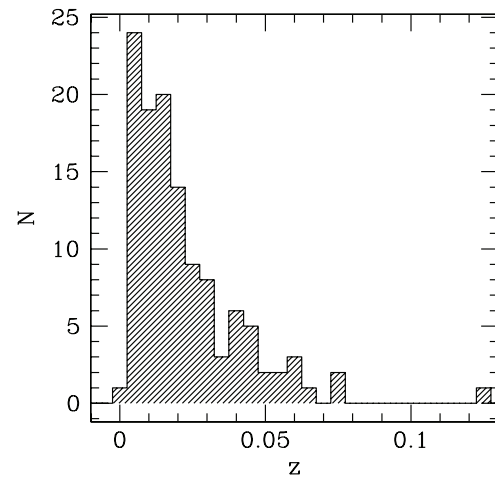


Figure 1. Redshift distribution of our sample containing 120 objects. The mean of the distribution is 0.0222, whereas the median is 0.0167.

classical starburst galaxies—spiral galaxies with HII nuclear regions or simply nuclear starburst galaxies—from the Montreal Blue Galaxy Survey (MBG; Coziol et al. 1993). However, the objects NGC 6970, IC 5154, ESO 533-G 014, and MCG -01-57-017 were presented only in a private list from Roger Coziol. Nuclear starburst galaxies are also often present in HII G lists due to their similar optical spectroscopic properties (for example, UM 477 and MRK 710). Thus our sample consists of 120 starburst regions in galaxies for which we have obtained line widths from optical high spectral resolution spectroscopy.

This sample is not complete in a statistical sense.¹ It is heterogeneous in nature comprising four orders of magnitude in $H\alpha$ luminosity range. Figure 1 shows the redshift distribution of our sample. The mean of the distribution is 0.022, and the median is 0.017. The study including all these galaxies is fundamental to investigating the range of the starburst magnitude for which the $L-\sigma$ relation is valid. This is, to date, the largest sample of HII Gs ever studied in order to test and calibrate the local $L-\sigma$ relation. This has been possible due to the private agreement between the Observatório Nacional-MCT and the European Southern Observatory (ESO) for the dedicated use of the 1.52 m and 2.2 m telescopes at La Silla, Chile.

2.2. High Spectral Resolution Spectroscopy

HII Gs are mostly compact objects and the young starburst regions in the cores of these systems dominate the main observational properties, i.e., emission line fluxes and their widths (Telles et al. 2001). More recently, in a spatially resolved kinematic study of the prototypical HII G II Zw 40, using three-dimensional integral field spectroscopy, Bordalo et al. (2009) confirmed that the line width measured in the nuclear core is the same as the line width measured over the whole extent of the starburst region, indicating that this kinematic core contains information about the overall dynamics of the warm gas.

We decided to use the Fiber-fed Extended Range Optical Spectrograph (FEROS) installed initially on the 1.52 m and, later, on the ESO 2.2 m telescope at La Silla Observatory in Chile, to observe galaxies for the first time, increasing our sample to the present 120 objects. The target fiber was positioned over the brightest region (nuclear core) of the galaxies. FEROS consists of two fibers coupled to the Cassegrain focus of the

¹ Definition of completeness for this class of emission line objects is rather tricky and a more detailed discussion of this issue is given in Salzer (1989).

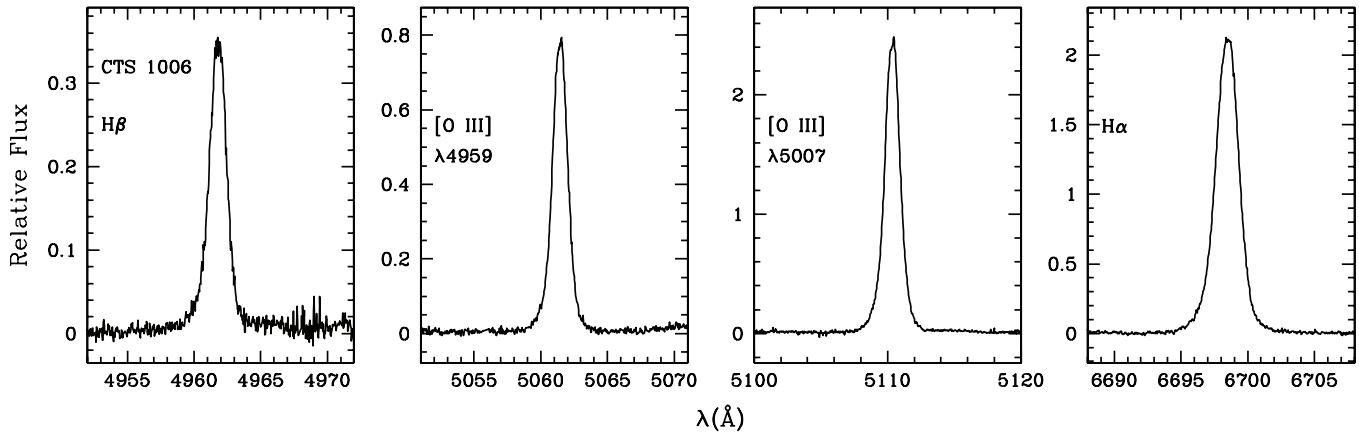


Figure 2. Optical wavelength calibrated spectrum of CTS 1006 obtained with the FEROS spectrograph. FEROS is an optical echelle spectrograph covering a wide range in wavelength, thus the most intense lines are shown in separated boxes.

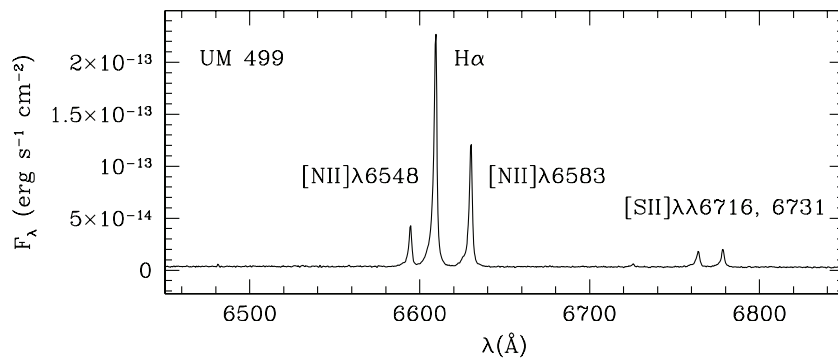


Figure 3. Optical calibrated spectrum of UM 499 obtained with the Coudé spectrograph.

telescope by micro lenses, providing a spectral resolution of $R = 48,000$ ($\sigma_{\text{inst}} = 2.50 \pm 0.20 \text{ km s}^{-1}$, $\sigma = \text{FWHM}/2.355$). Each of the two fibers has a projected $2''.7$ entrance aperture and the target and sky are recorded simultaneously.

The echelle FEROS spectrum covers the whole optical region 3560–9200 Å. We have observed 103 galaxies with this instrument in five observational runs in the period between 2000 November and 2007 April. The FEROS spectra were recorded in a 2048×4096 $15 \mu\text{m}$ pixel CCD. The basic reduction, extraction, and dispersion calibration of the spectra were done by a pipeline routine in MIDAS (François 1999). This routine processes bias and flat field calibration in a standard way and applies dispersion calibration to the object spectra from information from a thorium–argon–neon lamp spectrum. The final spectrum is calibrated only in wavelength. Line widths for Balmer H β (4861 Å), H α (6563 Å), and [O III] $\lambda\lambda 4959, 5007$ were measured for most of the galaxies observed. For four galaxies (Tol 0226-390, CTS 1004, Cam 08-28A, and CTS 1038), it was not possible to measure H α widths due to regions of bad pixels in the CCD. An example of a wavelength calibrated FEROS spectrum is shown in Figure 2.

Additional line widths were obtained with the 1.60 m telescope at Pico dos Dias Observatory (LNA/Brazil) using a Coudé spectrograph and the 600 l mm^{-1} diffraction grating, resulting in a spectral resolution at 6500 Å of 0.75 Å and 0.90 Å (instrumental FWHM) when CCD 48 and CCDs 101/106 were used, respectively. These correspond to $\sigma_{\text{inst}} = 14.7$ and 17.6 km s^{-1} , respectively. We observed in the region 6400–6900 Å to obtain line width measurements of the H α line emission. The slit

used was $1''$ for all observations. We obtained data from five observational runs between 1997 February and 1999 March.

Coudé data were reduced in a standard procedure for slit spectra in CCD using IRAF.² We used the CCDRED package for bias and flat field reduction and the SPECRED package for extraction and calibration procedures. We extracted the spectra from the brightest knot of the galaxies along the slit. An example of a calibrated Coudé spectrum is shown in Figure 3. The ASCII data files of all line profiles analyzed in this work are available at <http://www.on.br/astro/etelles/lsigma>.

Table 1 lists all observations including FEROS ones and observations with the spectrograph. Columns 1–3 give the galaxy name, and their coordinates (J2000). Columns 4–7 show the observation log for the Coudé spectrograph and Columns 8–10 show the observation log for the FEROS spectrograph, describing the total exposure times, number of exposures, the detector used (only for Coudé), and date of observations, respectively. Column 11 shows alternative names for the galaxy.

2.3. Spectrophotometry

Most of the spectrophotometric data used in this work come from KTC with 91 objects in common with our FEROS plus Coudé sample. Their data were obtained from a Boller & Chivens spectrograph on the 1.52 m ESO telescope. The spectra cover 4000 Å in the optical range centered at 5700 Å. They have a spectral resolution of 5 Å and the entrance slit was $2''$. KTC

² IRAF is distributed by the National Optical Astronomy Observatory, which is operated by the Association of Universities for Research in Astronomy, Inc., under cooperative agreement with the National Science Foundation.

Table 1
Journal of Observations

Galaxy	$\alpha(2000)$	$\delta(2000)$	Coudé				FEROS			Other Name
			Total Exp. Time (s)	Number of Exp.	Detector (CCD)	Obs. Date	Total Exp. Time (s)	Number of Exp.	Obs. Date	
UM 238	00 ^h 24 ^m 42 ^s .3	+01 ^d 44 ^m 02 ^s					3600	1	2001 Jul 21	
MBG 00463-0239	00 ^h 48 ^m 53 ^s .2	−02 ^d 22 ^m 55 ^s	3600	3	106	1998 Sep 13				MRK 557
UM 304	01 ^h 06 ^m 54 ^s .0	+01 ^d 56 ^m 44 ^s	5400	3	48	1997 Jul 28	5400	2	2000 Nov 23	
Tol 0104-388	01 ^h 07 ^m 02 ^s .1	−38 ^d 31 ^m 52 ^s					5400	1	2002 Jan 10	CTS 1001
UM 306	01 ^h 10 ^m 35 ^s .0	+02 ^d 06 ^m 51 ^s					5400	2	2000 Nov 23	
UM 307	01 ^h 11 ^m 30 ^s .7	+01 ^d 19 ^m 16 ^s	1800	1	48	1997 Jul 29				
UM 323	01 ^h 26 ^m 46 ^s .6	−00 ^d 38 ^m 46 ^s					5400	2	2000 Nov 21	
Tol 0127-397	01 ^h 29 ^m 15 ^s .8	−39 ^d 30 ^m 38 ^s	1200	1	106	1998 Sep 17	5400	1	2000 Nov 20	
Tol 0140-420	01 ^h 43 ^m 03 ^s .1	−41 ^d 49 ^m 41 ^s					5400	2	2000 Nov 24	
UM 137	01 ^h 46 ^m 23 ^s .9	+04 ^d 16 ^m 11 ^s					5400	1	2001 Jul 21	
UM 151	01 ^h 57 ^m 38 ^s .8	+02 ^d 25 ^m 24 ^s					3600	1	2001 Jul 21	MRK 1169
UM 382	01 ^h 58 ^m 09 ^s .3	−00 ^d 06 ^m 38 ^s					3600	1	2001 Jul 22	
MBG 01578-6806	01 ^h 59 ^m 06 ^s .0	−67 ^d 52 ^m 13 ^s	1200	1	106	1998 Sep 12				NGC 802
UM 391	02 ^h 03 ^m 30 ^s .4	+02 ^d 33 ^m 59 ^s	6000	5	106	1998 Sep 14	5400	2	2000 Nov 22	MRK 585
			2400	2	106	1998 Sep 15				
UM 395	02 ^h 06 ^m 56 ^s .8	+01 ^d 41 ^m 52 ^s					5400	2	2000 Nov 24	
UM 396	02 ^h 07 ^m 26 ^s .5	+02 ^d 56 ^m 55 ^s					5400	2	2000 Nov 22	
UM 408	02 ^h 11 ^m 23 ^s .4	+02 ^d 20 ^m 30 ^s					5400	2	2000 Nov 22	
UM 417	02 ^h 19 ^m 30 ^s .2	−00 ^d 59 ^m 11 ^s					4200	1	2001 Jul 22	
Tol 0226-390	02 ^h 28 ^m 12 ^s .3	−38 ^d 49 ^m 20 ^s	2400	2	106	1998 Sep 14	7200	2	2000 Nov 20	
CTS 1003	02 ^h 32 ^m 43 ^s .7	−39 ^d 34 ^m 27 ^s					5400	1	2002 Jan 9	Tol 0230-397
MBG 02411-1457	02 ^h 43 ^m 29 ^s .2	−14 ^d 45 ^m 16 ^s	4800	4	106	1998 Sep 12				NGC 1076
Tol 0242-387	02 ^h 44 ^m 37 ^s .9	−38 ^d 34 ^m 54 ^s					6300	1	2001 Jul 23	
CTS 1004	03 ^h 08 ^m 43 ^s .3	−40 ^d 24 ^m 28 ^s					5400	1	2002 Jan 9	Tol 0306-405
							4800	2	2000 Nov 23	
CTS 1005	03 ^h 59 ^m 08 ^s .9	−39 ^d 06 ^m 25 ^s					3600	1	2002 Jan 7	Cam 0357-3915
Tol 0440-381	04 ^h 42 ^m 08 ^s .1	−38 ^d 01 ^m 11 ^s	2400	2	106	1998 Sep 17	3600	2	2000 Nov 20	
CTS 1006	04 ^h 42 ^m 09 ^s .5	−45 ^d 25 ^m 12 ^s					3600	1	2002 Jan 10	
CTS 1007	04 ^h 46 ^m 49 ^s .4	−30 ^d 08 ^m 58 ^s					6000	2	2000 Nov 22	
CTS 1008	04 ^h 51 ^m 39 ^s .6	−31 ^d 53 ^m 06 ^s					7200	2	2000 Nov 21	
Tol 0505-387	05 ^h 07 ^m 00 ^s .8	−38 ^d 38 ^m 58 ^s					4800	2	2000 Nov 23	
Tol 0510-400	05 ^h 11 ^m 56 ^s .3	−39 ^d 59 ^m 47 ^s					5400	1	2002 Jan 9	
Tol 0528-383	05 ^h 29 ^m 57 ^s .4	−38 ^d 18 ^m 07 ^s					3600	2	2000 Nov 20	
II ZW 40	05 ^h 55 ^m 42 ^s .6	+03 ^d 23 ^m 32 ^s	3600	3	101	1997 Feb 5	4200	1	2000 Nov 21	
							900	1	2001 Mar 28	
Tol 0559-393	06 ^h 00 ^m 43 ^s .9	−39 ^d 19 ^m 07 ^s					3600	1	2000 Nov 23	
Tol 0610-387	06 ^h 12 ^m 14 ^s .2	−38 ^d 46 ^m 23 ^s					5400	2	2000 Nov 24	
Tol 0614-375	06 ^h 16 ^m 13 ^s .8	−37 ^d 36 ^m 37 ^s					3600	1	2007 Apr 16	
Tol 0633-415	06 ^h 35 ^m 10 ^s .2	−41 ^d 33 ^m 42 ^s					4800	2	2000 Nov 22	
							3600	1	2007 Apr 14	
Tol 0645-376	06 ^h 46 ^m 50 ^s .1	−37 ^d 43 ^m 22 ^s	1800	1	101	1997 Feb 4	2700	1	2000 Nov 20	
MRK 1201	07 ^h 25 ^m 45 ^s .7	+29 ^d 57 ^m 10 ^s					3600	1	2001 Mar 31	
Cam 0840+1201	08 ^h 42 ^m 20 ^s .9	+11 ^d 50 ^m 00 ^s					6000	2	2000 Nov 24	
Cam 0840+1044	08 ^h 42 ^m 36 ^s .6	+10 ^d 33 ^m 14 ^s					2700	1	2001 Mar 29	
Cam 08-28A	08 ^h 45 ^m 33 ^s .5	+16 ^d 05 ^m 46 ^s					1800	1	2001 Apr 1	MRK 702
MRK 710	09 ^h 54 ^m 49 ^s .5	+09 ^d 16 ^m 16 ^s	5400	3	101	1997 Feb 5	1800	1	2001 Apr 1	NGC 3049
MRK 711	09 ^h 55 ^m 11 ^s .3	+13 ^d 25 ^m 46 ^s					5400	1	2002 Jan 7	
Tol 0957-278	09 ^h 59 ^m 21 ^s .2	−28 ^d 08 ^m 00 ^s	7200	4	101	1997 Feb 6	1800	1	2001 Mar 28	Tol 2
Tol 1004-296NW	10 ^h 06 ^m 33 ^s .1	−29 ^d 56 ^m 09 ^s	1200	2	101	1998 Feb 3				
Tol 1004-296SE	10 ^h 06 ^m 33 ^s .1	−29 ^d 56 ^m 09 ^s	600	1	101	1998 Feb 3				
Tol 1008-286	10 ^h 10 ^m 18 ^s .1	−28 ^d 57 ^m 48 ^s					3600	1	2007 Apr 14	Tol 4
CTS 1011	10 ^h 19 ^m 21 ^s .2	−22 ^d 08 ^m 35 ^s					2700	1	2001 Apr 1	
CTS 1012	10 ^h 21 ^m 21 ^s .0	−21 ^d 36 ^m 27 ^s					3600	1	2007 Apr 14	
CTS 1013	10 ^h 25 ^m 05 ^s .9	−19 ^d 46 ^m 57 ^s					2700	1	2001 Mar 28	
Tol 1025-285	10 ^h 27 ^m 25 ^s .5	−28 ^d 47 ^m 33 ^s					5400	2	2001 Mar 29	Tol 6
Haro 24	10 ^h 27 ^m 55 ^s .4	+19 ^d 29 ^m 26 ^s					3600	1	2007 Apr 13	II Zw 47
CTS 1014	10 ^h 35 ^m 05 ^s .4	−27 ^d 20 ^m 08 ^s					4500	1	2007 Apr 14	Tol 1032-2704
CTS 1016	10 ^h 37 ^m 30 ^s .6	−24 ^d 08 ^m 41 ^s					3600	1	2001 Mar 31	
CTS 1017	10 ^h 37 ^m 40 ^s .4	−25 ^d 58 ^m 00 ^s					5400	1	2002 Jan 9	
CTS 1018	10 ^h 38 ^m 06 ^s .5	−26 ^d 21 ^m 56 ^s					3600	1	2001 Mar 31	
CTS 1019	10 ^h 41 ^m 03 ^s .7	−22 ^d 34 ^m 24 ^s					1800	1	2001 Apr 1	
CTS 1020	10 ^h 47 ^m 44 ^s .3	−20 ^d 57 ^m 49 ^s					2700	1	2001 Apr 1	

Table 1
(Continued)

Galaxy	$\alpha(2000)$	$\delta(2000)$	Coudé				FEROS			Other Name
			Total Exp. Time (s)	Number of Exp.	Detector (CCD)	Obs. Date	Total Exp. Time (s)	Number of Exp.	Obs. Date	
CTS 1022	10 ^h 48 ^m 40 ^s .2	−19 ^d 26 ^m 57 ^s					3600	1	2001 Mar 29	
[F80] 30	10 ^h 56 ^m 09 ^s .1	+06 ^d 10 ^m 22 ^s					1800	1	2001 Mar 31	MRK 1271, Tol 1053+064 Haro 4
MRK 36	11 ^h 04 ^m 58 ^s .3	+29 ^d 08 ^m 23 ^s					1800	1	2001 Mar 31	
UM 439	11 ^h 36 ^m 36 ^s .8	+00 ^d 48 ^m 58 ^s	3000	3	101	1998 Feb 4	3600	1	2007 Apr 13	
UM 448	11 ^h 42 ^m 12 ^s .4	+00 ^d 20 ^m 03 ^s	4800	4	101	1997 Feb 6	3600	1	2007 Apr 13	MRK 1304
Tol 1147-283	11 ^h 50 ^m 03 ^s .2	−28 ^d 40 ^m 17 ^s					3600	1	2001 Mar 28	Tol 17
UM 455	11 ^h 50 ^m 23 ^s .8	−00 ^d 31 ^m 41 ^s					2700	1	2001 Mar 31	
UM 456	11 ^h 50 ^m 36 ^s .3	−00 ^d 34 ^m 03 ^s					3600	1	2007 Apr 13	
UM 461	11 ^h 51 ^m 33 ^s .3	−02 ^d 22 ^m 22 ^s					1800	1	2001 Mar 31	
UM 463	11 ^h 52 ^m 47 ^s .5	−00 ^d 40 ^m 08 ^s					3600	1	2001 Apr 1	
CTS 1026	12 ^h 05 ^m 59 ^s .3	−27 ^d 00 ^m 56 ^s					3600	1	2007 Apr 14	
UM 477	12 ^h 08 ^m 11 ^s .1	+02 ^d 52 ^m 42 ^s	2400	3	101	1998 Feb 3	3600	1	2002 Jan 10	MRK 1466, NGC 4123
UM 483	12 ^h 12 ^m 14 ^s .7	+00 ^d 04 ^m 20 ^s					5400	1	2001 Jul 22	MRK 1313
CTS 1027	12 ^h 15 ^m 18 ^s .3	+05 ^d 45 ^m 40 ^s					3600	1	2007 Apr 16	Haro 6
MRK 1318	12 ^h 19 ^m 09 ^s .9	+03 ^d 51 ^m 21 ^s	1800	2	106	1999 Mar 14	3600	1	2001 Mar 29	Haro 8
CTS 1028	12 ^h 23 ^m 16 ^s .6	+04 ^d 50 ^m 09 ^s					3600	1	2001 Apr 1	Tol 1220+051, [F80] 34
UM 499	12 ^h 25 ^m 42 ^s .8	+00 ^d 34 ^m 21 ^s	2400	2	101	1997 Feb 4				
			1200	1	101	1997 Feb 5				
Tol 1223-359	12 ^h 25 ^m 46 ^s .9	−36 ^d 14 ^m 01 ^s					3600	1	2001 Mar 28	Tol 65
Haro 30	12 ^h 37 ^m 41 ^s .1	+27 ^d 07 ^m 46 ^s					3600	1	2007 Apr 13	MRK 650, IC 3600
[SC98] 01	13 ^h 04 ^m 15 ^s .2	−22 ^d 52 ^m 53 ^s					3600	1	2001 Mar 29	
CTS 1029	13 ^h 06 ^m 05 ^s .1	−22 ^d 37 ^m 22 ^s					6300	2	2001 Mar 30	[SC98] 09
[SC98] 11	13 ^h 06 ^m 19 ^s .3	−22 ^d 58 ^m 49 ^s					4500	1	2007 Apr 16	
UM 559	13 ^h 17 ^m 42 ^s .8	−01 ^d 00 ^m 01 ^s					3600	1	2001 Mar 28	
[SC98] 68	13 ^h 21 ^m 50 ^s .0	−22 ^d 28 ^m 31 ^s					3600	1	2001 Mar 31	
UM 570	13 ^h 23 ^m 47 ^s .4	−01 ^d 32 ^m 52 ^s					4500	1	2001 Jul 22	
[SC98] 88	13 ^h 25 ^m 33 ^s .0	−26 ^d 02 ^m 50 ^s					4500	1	2001 Mar 29	
CTS 1030	13 ^h 25 ^m 33 ^s .3	−25 ^d 55 ^m 33 ^s					3600	1	2007 Apr 14	[SC98] 84
POX 186	13 ^h 25 ^m 48 ^s .6	−11 ^d 36 ^m 38 ^s					4500	1	2001 Apr 1	
							4500	1	2007 Apr 13	
CTS 1031	13 ^h 25 ^m 58 ^s .5	−23 ^d 38 ^m 09 ^s					4500	1	2007 Apr 16	[SC98] 91
Tol 1345-420	13 ^h 48 ^m 22 ^s .2	−42 ^d 21 ^m 15 ^s	600	1	106	1999 Mar 14	3600	1	2001 Mar 30	Tol 111
CTS 1033	13 ^h 49 ^m 44 ^s .8	−18 ^d 11 ^m 28 ^s					3600	1	2007 Apr 13	
Tol 1400-397	14 ^h 03 ^m 05 ^s .7	−40 ^d 02 ^m 28 ^s					7200	1	2001 Jul 23	Tol 115
UM 649	14 ^h 14 ^m 27 ^s .7	−00 ^d 28 ^m 08 ^s					5400	1	2001 Jul 21	
CTS 1034	14 ^h 19 ^m 32 ^s .4	−27 ^d 35 ^m 08 ^s					5400	2	2001 Mar 28	
II ZW 70	14 ^h 50 ^m 56 ^s .5	+35 ^d 34 ^m 18 ^s					1400	1	2001 Mar 28	MRK 829
CTS 1035	14 ^h 57 ^m 19 ^s .7	−22 ^d 23 ^m 35 ^s					3600	1	2001 Mar 30	
							3600	1	2001 Mar 31	
CTS 1037	15 ^h 15 ^m 44 ^s .0	−18 ^d 18 ^m 52 ^s					4300	1	2007 Apr 13	
Cam 1543+0907	15 ^h 45 ^m 38 ^s .6	+09 ^d 03 ^m 28 ^s					3600	1	2001 Mar 31	
Tol 1924-416	19 ^h 27 ^m 58 ^s .2	−41 ^d 34 ^m 32 ^s	3600	2	48	1997 Jul 28				
Tol 1939-419	19 ^h 33 ^m 32 ^s .0	−41 ^d 50 ^m 56 ^s					3100	1	2007 Apr 16	
Tol 1937-423	19 ^h 40 ^m 58 ^s .6	−42 ^d 15 ^m 45 ^s	2400	2	106	1998 Sep 16	5400	1	2001 Jul 21	
CTS 1038	19 ^h 54 ^m 52 ^s .6	−32 ^d 56 ^m 40 ^s					4500	1	2001 Apr 1	
CTS 1039	20 ^h 05 ^m 51 ^s .3	−45 ^d 28 ^m 42 ^s					3600	1	2007 Apr 16	
Tol 2010-382	20 ^h 14 ^m 06 ^s .4	−38 ^d 07 ^m 41 ^s	5400	3	48	1997 Jul 29	3600	1	2007 Apr 14	
Tol 2019-405	20 ^h 23 ^m 06 ^s .2	−40 ^d 20 ^m 33 ^s					5400	1	2001 Jul 21	
Tol 2041-394	20 ^h 44 ^m 50 ^s .8	−39 ^d 13 ^m 17 ^s					5400	1	2001 Jul 22	
NGC 6970	20 ^h 52 ^m 09 ^s .4	−48 ^d 46 ^m 40 ^s	2400	2	48	1997 Jul 28				
MBG 20533-4410	20 ^h 56 ^m 43 ^s .4	−43 ^d 59 ^m 10 ^s	4800	4	48	1997 Jul 28				NGC 6983
Tol 2122-408	21 ^h 25 ^m 46 ^s .9	−40 ^d 39 ^m 12 ^s	4800	4	106	1998 Sep 16	3600	1	2000 Nov 21	
Tol 2138-405	21 ^h 41 ^m 21 ^s .8	−40 ^d 19 ^m 06 ^s					5400	1	2001 Jul 23	
Tol 2138-397	21 ^h 41 ^m 38 ^s .4	−39 ^d 31 ^m 30 ^s					1800	1	2007 Apr 16	
Tol 2146-391	21 ^h 49 ^m 48 ^s .2	−38 ^d 54 ^m 09 ^s					5400	1	2001 Jul 21	
MBG 21567-1645	21 ^h 59 ^m 26 ^s .1	−16 ^d 30 ^m 44 ^s	5400	3	48	1997 Jul 29				NGC 7165
MBG 22012-1550	22 ^h 03 ^m 56 ^s .3	−15 ^d 36 ^m 00 ^s	5400	3	48	1997 Jul 29				
IC 5154	22 ^h 04 ^m 30 ^s .3	−66 ^d 06 ^m 45 ^s	2400	2	106	1998 Sep 12				
ESO 533-G 014	22 ^h 19 ^m 50 ^s .6	−26 ^d 20 ^m 30 ^s	3600	3	106	1998 Sep 12				
MCG -01-57-017	22 ^h 38 ^m 13 ^s .5	−07 ^d 02 ^m 05 ^s	2400	2	106	1998 Sep 14				
Tol 2240-384	22 ^h 43 ^m 32 ^s .4	−38 ^d 11 ^m 24 ^s					5400	1	2001 Jul 22	
							3600	1	2001 Jul 23	

Table 1
(Continued)

Galaxy	$\alpha(2000)$	$\delta(2000)$	Coudé				FEROS			Other Name
			Total Exp. Time (s)	Number of Exp.	Detector (CCD)	Obs. Date	Total Exp. Time (s)	Number of Exp.	Obs. Date	
MBG 23121-3807	23 ^h 14 ^m 52 ^s .3	−37 ^d 51 ^m 20 ^s	8700	8	106	1998 Sep 11				
Tol 2326-405	23 ^h 28 ^m 49 ^s .4	−40 ^d 15 ^m 26 ^s					4500	1	2001 Jul 23	
UM 167	23 ^h 36 ^m 14 ^s .1	+02 ^d 09 ^m 19 ^s	3600	2	48	1997 Jul 29				MRK 538, NGC 7714
UM 191	23 ^h 56 ^m 59 ^s .6	−02 ^d 05 ^m 02 ^s	5400	3	48	1997 Jul 29	7200	2	2000 Nov 21	MRK 542
			2400	2	106	1998 Sep 13				
			4800	4	106	1998 Sep 14				

observed with a long slit and in some cases extracted more than one spectrum for a galaxy, representing different bright regions spatially separated. Additional and complementary data were obtained from recent works. Emission line fluxes and equivalent widths of permitted and forbidden line fluxes were gathered from these sources to derive the physical parameters such as extinction coefficient, ionization ratio, electron temperature and density, and oxygen abundance.

3. RESULTS

3.1. Line Widths and Velocity Dispersions

We have measured the emission line widths from our high spectral resolution observations by fitting single Gaussians to the observed line profiles using the SPLIT routine of IRAF. The H α line for the Coudé spectra was measured and H α , H β , and [O III] $\lambda\lambda 4959, 5007$ lines for FEROS spectra were detected and measured for almost all galaxies. All observed FWHM, uncorrected for instrumental width, are presented in Table 2.

In several cases, a single Gaussian fit did not adequately represent the observed profile. Some present irregularities such as prominent wings and multiple components (see also Relaño et al. 2005). Different methodologies to obtain line widths such as multiple Gaussians or Gauss–Hermite (Riffel 2010, and references therein) fits are viable approaches to the problem of modeling real emission line profiles and were tested. For instance, Gauss–Hermite fits provide single width measurements that are comparable to single Gaussian fit measurements, and they are less sensitive to small asymmetries. In the case of profiles with a dominant broad component or with double peaks, multiple Gaussians or Gauss–Hermite methodologies provide better fits. However, the interpretation of the model parameters is not obvious. Further detailed analysis with more data is needed to resolve this issue, but it is beyond the scope of this paper. Here, we are interested in the simplest methodology to measure the line widths that may provide us with a robust kinematic measurement of the starburst region as a whole.

As a simple alternative to deal with this problem, we classified galaxies depending on their line profiles using the following criteria.

1. *Gaussian profile.* Symmetrical lines well represented by a single Gaussian fit. These profiles occur in 62% of galaxies in our sample.
2. *Irregular profile.* Asymmetrical lines showing prominent wings and generally peaked. These occur in 29% of our sample.
3. *Profile with components.* These clearly show more than one component in emission, normally double-peak lines with similar intensities, occurring in 17% of our sample.

Our classification was done by eye comparison between the single Gaussian fit and the observed line profile, therefore it has an intrinsic subjectiveness though it is interesting for early and qualitative purposes in this work. Since for most galaxies we have the four strong emission lines, we checked them all to classify the galaxies. Figure 4 presents some examples of prototypical H α profiles of the three classes defined. All galaxies were classified including those showing low signal-to-noise ratio (S/N) in their emission line profiles. Some galaxies may have been classified as presenting Gaussian profiles simply because the line wings were not well sampled. The spectra from FEROS were used in priority to Coudé ones to classify those galaxies observed with both instruments. The galaxies were assigned a letter G for Gaussian, I for irregular profiles, and C for profiles with components. The respective class for each galaxy is shown in the last column of Table 2. We will return to this point later in Section 4.2 using a semi-quantitative analysis of line profile classifications to select a more homogeneous sample.

We derived the radial velocity dispersions (σ) from the observed FWHMs presented in Table 2. The observed velocity dispersions (σ_{obs}) in km s^{−1} were corrected by the instrumental (σ_{inst}), and thermal broadening (σ_{th}), assuming a Maxwellian velocity distribution of the hydrogen and oxygen atoms,

$$\sigma_{\text{th}} = \sqrt{\frac{kT_e}{m}},$$

where k is the Boltzmann constant, T_e is the electronic temperature in Kelvin, and m is the mass of the atom. We used $T_e(\text{O III})$ presented in Table 3 to derive σ_{th} for all galaxies. For those galaxies where T_e was not directly determined or found in the literature, we assumed a mean value of 14,000 K. For H lines from FEROS spectra, we also corrected σ_{obs} by the fine structure broadening (σ_{fs}): 3.20 km s^{−1} for H α and 2.40 km s^{−1} for H β as adopted by García-Díaz et al. (2008). The velocity dispersion of interest here, sometimes called the “non-thermal” velocity dispersion, was calculated by

$$\sigma = \sqrt{\sigma_{\text{obs}}^2 - \sigma_{\text{inst}}^2 - \sigma_{\text{th}}^2 - \sigma_{\text{fs}}^2}.$$

For FEROS, $\sigma_{\text{inst}} = 2.5$ km s^{−1}, while for Coudé, $\sigma_{\text{inst}} = 14.7$ km s^{−1} and $= 17.6$ km s^{−1}, depending on the instrumentation used (see Section 2.2). The correction due to σ_{th} for H lines varies between 9.5 and 12.5 km s^{−1}, and for the O lines, between 2 and 3 km s^{−1}. We estimated the error in σ due to uncertainties in T_e as being $\delta\sigma_{\text{H}} < 0.3$ km s^{−1} and $\delta\sigma_{\text{O}} < 0.1$ km s^{−1}.

The internal errors were determined as a function of the S/N calculated for the emission lines and defined as the ratio between the peak intensity and the adjacent continuum rms. Figure 5 shows a comparison between σ derived from the same

Table 2
Measurements of Redshifts, Distances, and Line Widths from FEROS and Coudé Spectra

Galaxy	z_{hel}	D Mpc	FWHM $H\beta$	FWHM [O III] 4959 Å	FWHM [O III] 5007 Å	FWHM $H\alpha$	FWHM $H\alpha$ (Coudé)	Class
UM 238	0.01427	55.3	0.844	0.775	0.785	1.158	...	G
MBG 00463-0239	0.01328	51.4	3.200	I
UM 304	0.01570	61.7	3.063	3.556	3.444	4.140	4.107	C
Tol 0104-388	0.02263	92.4	1.914	1.880	1.988	2.618	...	I
UM 306	0.01649	65.1	0.846	0.703	0.736	1.147	...	G
UM 307	0.02249	90.4	2.772	G
UM 323	0.00648	23.0	0.873	0.853	0.786	1.143	...	G'
Tol 0127-397	0.01735	70.3	1.510	1.420	1.440	1.950	2.045	G'
Tol 0140-420	0.02205	89.9	1.193	1.092	1.104	1.510	...	C
UM 137	0.00591	20.8	0.676	0.962	...	G
UM 151	0.01607	63.9	1.196	0.892	1.066	1.760	...	G
UM 382	0.01206	47.0	0.812	0.772	0.742	1.028	...	G
MBG 01578-6806	0.00490	19.8	1.669	G
UM 391	0.02101	84.9	2.291	...	3.188	3.168	3.320	C
UM 395	0.02234	90.6	1.255	1.281	1.206	1.711	...	G'
UM 396	0.02078	84.0	1.134	1.099	1.110	1.517	...	G'
UM 408	0.01153	45.0	0.867	0.661	0.681	1.165	...	G'
UM 417	0.00872	33.3	0.639	0.544	0.606	0.994	...	G'
Tol 0226-390	0.04771	199.2	3.620	3.410	3.346	...	4.219	I
CTS 1003	0.01684	68.9	1.055	1.005	1.000	1.452	...	G
MBG 02411-1457	0.00686	26.1	2.047	G
Tol 0242-387	0.12635	531.5	4.252	4.966	4.949	5.664	...	I
CTS 1004	0.04734	198.3	1.804	1.780	1.831	I
CTS 1005	0.07441	313.3	2.082	1.963	1.964	2.772	...	I
Tol 0440-381	0.04082	172.2	1.440	1.308	1.310	1.967	2.776	C
CTS 1006	0.02072	87.5	1.492	1.341	1.360	2.032	...	G'
CTS 1007	0.04130	174.2	1.255	1.123	1.108	1.648	...	G'
CTS 1008	0.06106	257.7	2.030	1.891	1.910	2.693	...	G'
Tol 0505-387	0.02897	122.6	0.967	0.812	0.906	1.269	...	G'
Tol 0510-400	0.04132	174.9	1.425	1.282	1.281	1.795	...	G'
Tol 0528-383	0.01163	49.8	0.826	0.760	0.794	1.188	...	G'
II ZW 40	0.00258	11.8	1.329	1.277	1.300	1.826	1.951	I
Tol 0559-393	0.04478	190.3	2.073	1.713	1.929	2.677	...	G
Tol 0610-387	0.00575	25.7	0.771	...	0.929	1.199	...	G
Tol 0614-375	0.03157	134.8	1.820	2.045	2.036	2.646	...	G'
Tol 0633-415	0.01640	71.1	1.310	1.223	1.251	1.705	...	G'
Tol 0645-376	0.02579	110.9	1.229	1.228	1.198	1.708	1.670	G'
MRK 1201	0.01857	80.6	1.843	2.491	...	G
Cam 0840+1201	0.02938	128.2	1.510	1.397	1.400	1.945	...	G'
Cam 0840+1044	0.01044	48.0	0.752	0.549	0.573	0.999	...	G'
Cam 08-28A	0.05304	227.8	2.090	1.797	1.856	I
MRK 710	0.00502	25.9	2.201	...	2.127	2.708	2.697	C
MRK 711	0.01944	86.7	3.685	3.418	3.499	5.046	...	I
Tol 0957-278	0.00334	18.8	1.031	1.051	1.044	1.503	1.543	I
Tol 1004-296NW	0.00370	20.2	1.943	I
Tol 1004-296SE	0.00359	19.8	1.738	G
Tol 1008-286	0.01384	63.1	1.054	1.010	1.008	1.455	...	G'
CTS 1011	0.01207	55.9	0.921	0.823	0.837	1.241	...	G'
CTS 1012	0.01089	50.9	0.787	0.650	0.646	1.051	...	G'
CTS 1013	0.02688	118.5	1.390	1.346	1.380	1.774	...	C
Tol 1025-285	0.03073	134.5	2.356	...	2.438	2.986	...	G
Haro 24	0.04327	187.3	1.770	1.587	1.759	2.565	...	I
CTS 1014	0.05895	253.8	2.333	1.778	1.849	2.803	...	I
CTS 1016	0.03450	150.6	1.456	1.323	1.410	2.203	...	I
CTS 1017	0.03544	154.5	1.186	1.176	1.176	1.598	...	G'
CTS 1018	0.03925	170.6	1.453	1.313	1.316	1.977	...	G
CTS 1019	0.06651	285.8	1.888	1.895	1.936	2.761	...	G'
CTS 1020	0.01248	57.7	1.393	1.365	1.399	1.911	...	G'
CTS 1022	0.01369	62.9	0.974	0.839	0.854	1.427	...	G
[F80] 30	0.00335	18.2	0.903	0.741	0.749	1.205	...	G'
MRK 36	0.00212	13.2	0.782	0.687	0.717	1.051	...	G'
UM 439	0.00382	21.3	0.805	0.708	0.711	1.103	1.444	G'
UM 448	0.01834	82.6	2.947	3.043	3.017	4.143	3.376	C
Tol 1147-283	0.00626	31.2	0.793	0.799	0.724	1.113	...	G'

Table 2
(Continued)

Galaxy	z_{hel}	D Mpc	FWHM $H\beta$	FWHM [O III] 4959 Å	FWHM [O III] 5007 Å	FWHM $H\alpha$	FWHM $H\alpha$ (Coudé)	Class
UM 455	0.01306	60.3	0.998	0.746	0.740	1.518	...	I
UM 456	0.00572	29.3	0.757	0.631	0.643	1.017	...	G'
UM 461	0.00352	20.0	0.669	0.512	0.519	0.912	...	G'
UM 463	0.00468	24.9	0.849	0.680	0.676	1.057	...	G'
CTS 1026	0.00577	29.2	1.710	1.689	1.705	2.284	...	G
UM 477	0.00422	22.8	2.243	...	2.860	3.019	3.038	C
UM 483	0.00792	38.4	0.816	0.776	0.744	1.105	...	I
CTS 1027	0.00674	33.4	0.892	0.799	0.821	1.217	...	I
MRK 1318	0.00504	26.2	0.756	0.680	0.695	1.052	1.448	G'
CTS 1028	0.01776	79.9	1.141	1.074	1.098	1.520	...	C
UM 499	0.00707	34.8	2.520	I
Tol 1223-359	0.00930	44.2	0.828	0.681	0.707	1.163	...	G'
Haro 30	0.01552	69.5	1.746	1.887	1.845	2.428	...	I
[SC98] 01	0.01041	48.4	0.975	0.791	0.720	1.185	...	G'
CTS 1029	0.03633	157.8	1.787	...	G
[SC98] 11	0.03104	135.5	1.317	1.285	1.244	1.801	...	I
UM 559	0.00429	22.5	0.794	0.676	0.687	1.103	...	G'
[SC98] 68	0.02377	104.7	1.274	1.346	1.300	1.758	...	G
UM 570	0.02249	99.3	0.930	0.884	0.867	1.291	...	G'
[SC98] 88	0.01454	65.6	1.066	0.896	0.860	1.491	...	I
CTS 1030	0.01505	67.7	1.221	1.213	1.212	1.668	...	C
POX 186	0.00415	21.9	0.715	0.584	0.586	0.984	...	G'
CTS 1031	0.04525	195.3	1.338	1.296	1.386	1.770	...	I
Tol 1345-420	0.00807	37.5	0.877	0.743	0.791	1.188	1.655	G'
CTS 1033	0.01549	69.4	1.921	1.935	1.939	2.602	...	C
Tol 1400-397	0.03101	134.3	1.352	1.299	1.368	1.922	...	G'
UM 649	0.02611	113.9	1.152	0.935	1.018	1.480	...	G
CTS 1034	0.02292	100.2	...	1.091	1.037	1.533	...	G
II ZW 70	0.00406	19.2	0.901	0.794	0.823	1.377	...	G'
CTS 1035	0.02848	123.2	1.164	1.120	1.086	1.409	...	G
CTS 1037	0.02130	92.5	1.562	1.530	1.513	2.074	...	I
Cam 1543+0907	0.03766	160.8	1.293	1.186	1.179	1.716	...	G'
Tol 1924-416	0.00952	38.4	2.065	I
Tol 1939-419	0.02525	104.8	0.962	1.336	...	G
Tol 1937-423	0.00932	37.4	1.022	0.768	0.888	1.262	1.874	G
CTS 1038	0.04984	208.0	...	2.123	2.136	I
CTS 1039	0.04486	187.4	1.693	1.704	1.722	2.287	...	I
Tol 2010-382	0.02026	83.0	1.506	...	1.480	1.899	2.166	G'
Tol 2019-405	0.01495	60.6	1.095	0.978	0.996	1.300	...	I
Tol 2041-394	0.02576	106.0	...	1.178	1.121	1.627	...	G
NGC 6970	0.01751	71.6	2.594	C
MBG 20533-4410	0.01714	69.7	3.075	C
Tol 2122-408	0.01480	59.4	1.114	1.052	1.071	1.416	1.717	G
Tol 2138-405	0.05802	241.7	2.445	2.468	2.496	3.444	...	C
Tol 2138-397	0.01570	63.0	0.996	0.998	0.900	1.391	...	G'
Tol 2146-391	0.02953	121.3	1.154	0.935	0.991	1.503	...	I
MBG 21567-1645	0.01738	68.8	5.513	C
MBG 22012-1550	0.04227	173.9	5.074	C
IC 5154	0.01068	43.7	2.035	G
ESO 533-G 014	0.00873	32.6	1.317	G
MCG -01-57-017	0.00962	35.6	1.567	G
Tol 2240-384	0.07584	316.6	2.082	2.112	2.196	2.940	...	C
MBG 23121-3807	0.00945	36.2	1.777	G
Tol 2326-405	0.05515	229.3	1.556	2.456	...	I
UM 167	0.00928	34.0	3.925	G
UM 191	0.02427	97.4	1.265	...	1.584	1.798	2.000	G'

Note. The last column indicates the class of the galaxies discussed in the text.

ion considering all data. The FEROS measurements are very consistent. The rms of a linear fit for all points is 1.96 for $H\text{II}$ and 1.36 for [O III] lines in km s^{-1} (Figure 5, left and center). The comparison between FEROS and Coudé measurements also

shows good agreement except for two objects (Tol 0440-381 and UM 448) that present components in their line profiles. The observation of these objects is more sensitive to the position of the slit and fiber over the galaxy. The rms = 5.22 km s^{-1} from

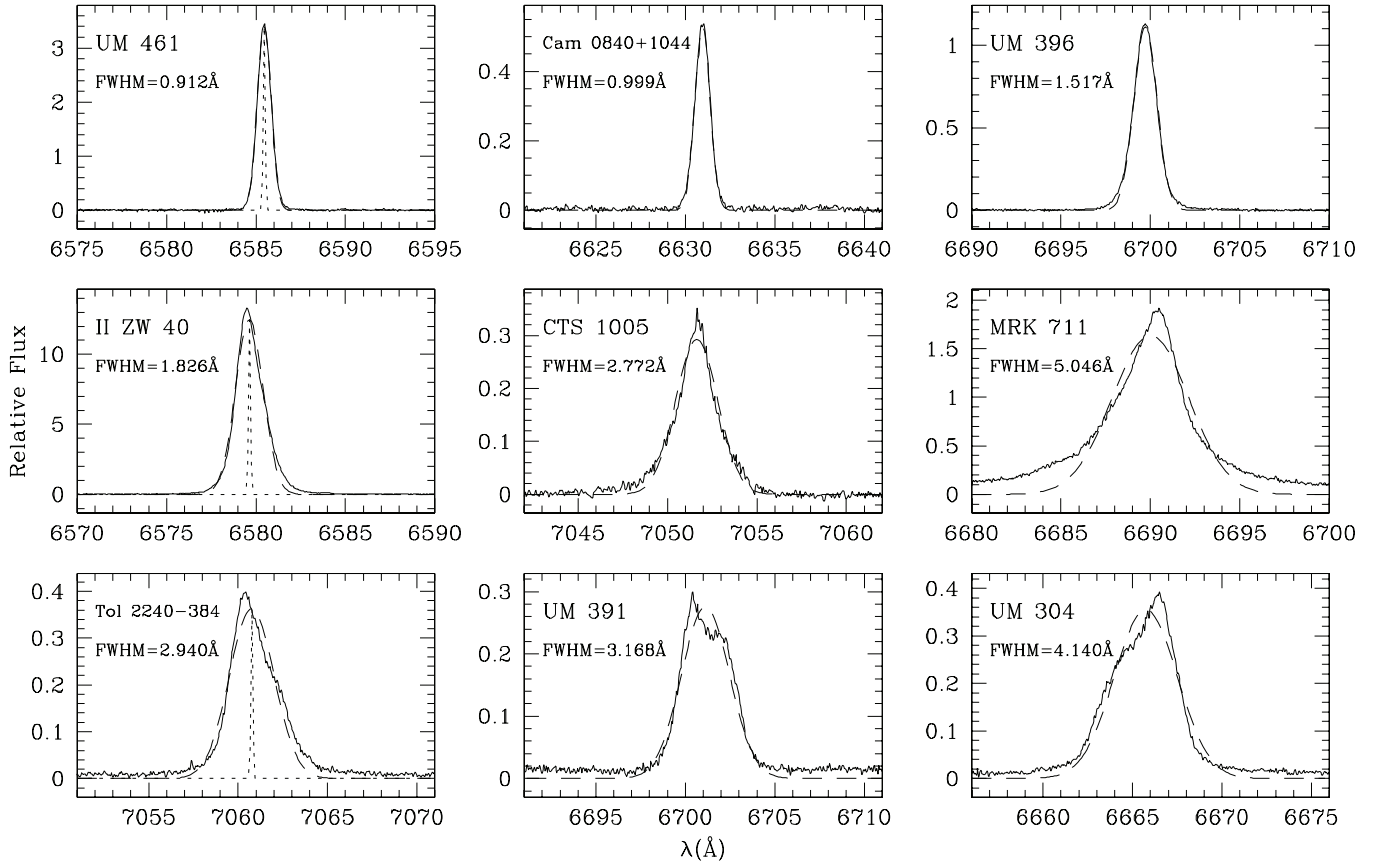


Figure 4. Examples of the three classes of line profiles visually identified. First row: galaxies with nearly Gaussian profiles; second row: galaxies with irregular profiles; and third row: galaxies with line profiles clearly showing components. The dotted narrow lines in all of the left-hand boxes represent the FEROS instrumental profile, $\sigma_{\text{inst}} = 2.50 \text{ km s}^{-1}$. The dashed lines represent single Gaussian fits to the observed profiles.

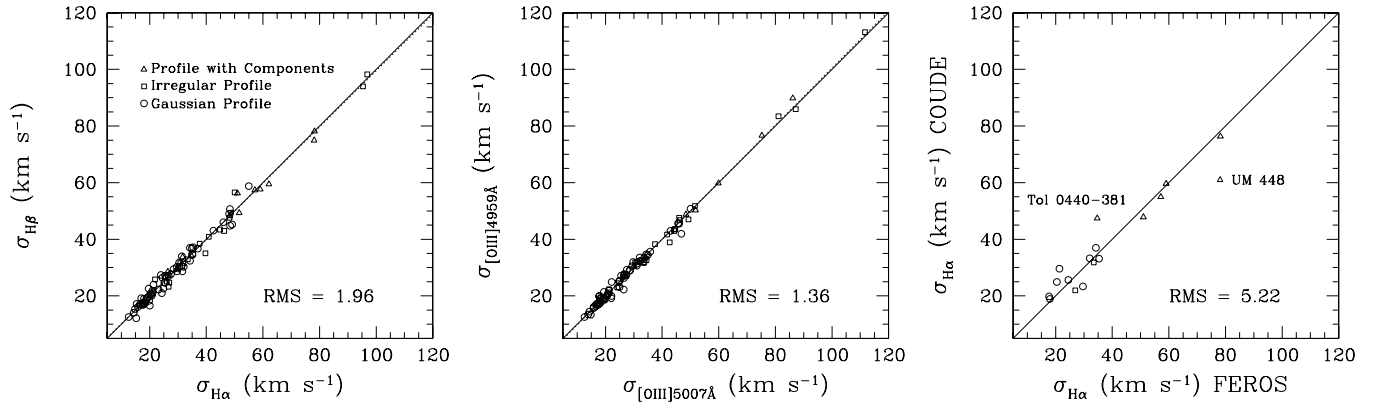


Figure 5. Left: testing the consistency of measurements between σ derived from $H\alpha$ and $H\beta$ (FEROS); (center) $\sigma_{[\text{O III}]\lambda 4959\text{\AA}}$ and $\sigma_{[\text{O III}]\lambda 5007\text{\AA}}$. Right: $H\alpha$ from FEROS (x) and Coudé (y). Tol 0440-381 and UM 448, noted in the right plot, present the most discrepant measurements possibly due to different positions covered by the observations.

a linear fit is also shown inside the box (Figure 5, right). For different ranges of S/N, we selected samples of galaxies for their σ values to be compared. The selection was based on the S/N of the weaker lines of each ion (i.e., $H\beta$ and $[\text{O III}]\lambda 4959$) and their σ values were plotted in the y-axis against the σ values derived from the more intense line in x . The errors were estimated by taking the rms of a direct least-squares fit for each data set. In a similar procedure, we estimated the errors for Coudé $\sigma_{H\alpha}$ comparing sets of two ranges of S/N with $\sigma_{H\alpha}$ of galaxies also observed with FEROS. Table 4 shows the estimated errors in σ as a function of S/N for H and O lines. The σ values and their respective errors for each line are shown in Table 5.

3.2. Physical Conditions

Before we use line fluxes to derive physical conditions, we need to infer the amount of extinction for each galaxy. Dust in starburst regions is responsible for extinction of light in the line of sight due to absorption and scattering. In optical wavelengths, the amount of extinction can be reasonably well estimated from H recombination lines through the Balmer Decrement method. To derive the $H\beta$ extinction coefficient ($C_{H\beta}$) for galaxies with KTC spectrophotometry, we used the theoretical ratios $H\alpha/H\beta = 2.87$ and $H\gamma/H\beta = 0.466$ for case B, optically thick with $T = 10^4 \text{ K}$ (Osterbrock 1989). In cases where $H\alpha/H\beta$ was

Table 3H α Integrated Fluxes, H β Extinction Coefficients, H β Equivalent Widths, Ionization Ratios [O III]/[O II], O/H Ratios and Electron Densities, and Temperatures

Galaxy	$F_{H\alpha}$ (erg s $^{-1}$ cm $^{-2}$)	$C_{H\beta}$	$W_{H\beta}$ (Å)	[O III]/[O II]	N_e (cm $^{-3}$)	T_e (10 4 K)	12+ log(O/H)	Ref.
UM 238	2.0e-14	0.23	36	3.31	867	1.53	7.89	1,1,1,1,1,18
MBG 00463-0239	8.2e-14	0.38	10	0.19	374	1.40	8.70	1,1,1,1,1,22,16
UM 304	1.5e-13	1.09	204	1.40	...	14,2,-,-,22,22,-
Tol 0104-388	4.7e-14	0.19	60	1.14	846	1.49	7.96	1,1,1,1,1,18
UM 306	3.1e-14	0.08	24	2.21	27	1.16	8.18	1,1,1,1,1,18
UM 307	1.1e-13	0.25	23	0.67	983	1.40	8.43	1,1,1,1,1,22,16
UM 323	2.6e-14	0.85	21	0.90	27	1.76	7.92	1,1,1,1,1,18
Tol 0127-397	4.1e-14	0.51	204	1.40	...	14,2,-,-,22,22,-
Tol 0140-420	2.3e-14	0.00	56	1.98	27	1.28	8.06	1,1,1,1,1,18
UM 137	1.5e-14	0.37	4	0.55	27	1.40	8.25	1,1,1,1,1,22,17
UM 151	2.6e-14	0.41	20	0.79	94	1.40	8.47	1,1,1,15,1,22,17
UM 382	1.9e-14	0.18	135	10.90	45	1.62	7.82	6,6,6,6,6,6,6
MBG 01578-6806	204	1.40	...	-, -, -, -, 22,22,-
UM 391	5.1e-14	0.54	14	0.35	27	1.40	8.40	1,1,1,1,1,22,16
UM 395	1.6e-14	0.49	6	0.42	579	1.40	8.63	1,1,1,1,1,22,17
UM 396	3.7e-14	0.00	153	5.85	27	1.22	8.18	1,1,1,1,1,18
UM 408	2.0e-14	0.06	33	3.66	207	1.33	8.02	1,1,1,1,1,18
UM 417	5.8e-15	0.45	46	7.65	27	1.40	8.04	1,1,1,1,1,22,17
Tol 0226-390	1.0e-13	0.31	115	3.03	193	1.16	8.15	1,1,1,1,1,18
CTS 1003	2.2e-14	0.24	204	1.40	7.90	3,3,-,-,22,22,3
MBG 02411-1457	4.7e-14	0.76	2	0.15	132	1.40	8.26	1,1,1,1,1,22,16
Tol 0242-387	1.1e-13	0.78	204	1.40	8.23	2,2,-,-,22,22,19
CTS 1004	3.5e-14	0.00	77	3.83	101	1.21	8.14	1,1,1,1,1,18
CTS 1005	4.3e-14	0.16	134	11.14	204	1.46	7.91	1,1,1,1,22,1,18
Tol 0440-381	5.5e-14	0.11	29	1.77	27	1.53	7.96	1,1,1,1,1,18
CTS 1006	1.4e-13	0.15	70	2.88	27	1.28	8.04	1,1,1,1,1,18
CTS 1007	4.3e-14	0.01	204	1.40	7.83	3,3,-,-,22,22,3
CTS 1008	5.7e-14	0.24	140	6.04	278	1.21	8.16	1,1,1,1,1,18
Tol 0505-387	1.1e-14	0.35	10	0.66	27	1.40	8.50	1,1,1,1,1,22,17
Tol 0510-400	3.3e-14	0.19	64	2.39	227	1.40	8.25	1,1,1,1,1,22,16
Tol 0528-383	3.7e-14	0.35	21	1.86	133	1.48	7.96	1,1,1,1,1,18
II ZW 40	3.5e-13	0.61	184	10.98	217	1.31	8.07	1,1,1,1,1,18
Tol 0559-393	4.5e-14	0.35	204	1.40	...	2,2,-,-,22,22,-
Tol 0610-387	1.1e-14	0.93	4	0.44	27	1.40	8.56	1,1,1,2,1,22,17
Tol 0614-375	6.9e-14	1.25	204	1.40	7.86	2,2,-,-,22,22,20
Tol 0633-415	1.1e-13	0.40	83	4.59	67	1.25	8.14	1,1,1,21,1,21,4
Tol 0645-376	2.9e-14	0.19	28	1.58	27	1.78	7.77	1,1,1,1,1,18
MRK 1201	3.9e-14	0.52	8	0.50	1467	1.40	9.36	1,1,1,1,1,22,16
Cam 0840+1201	1.1e-13	0.03	105	3.53	27	1.32	7.98	1,1,1,1,1,18
Cam 0840+1044	2.1e-14	0.25	44	7.85	27	1.58	7.73	1,1,1,1,1,18
Cam 08-28A	1.5e-13	0.28	37	1.60	97	1.11	8.13	1,1,1,1,1,18
MRK 710	4.5e-13	0.50	29	0.23	184	1.40	8.95	1,1,1,1,1,22,16
MRK 711	1.9e-13	0.54	28	1.61	460	1.40	8.79	1,1,1,2,1,22,17
Tol 0957-278	2.0e-13	0.17	36	1.92	74	1.24	8.02	1,1,1,1,1,18
Tol 1004-296NW	7.4e-13	0.40	62	3.50	122	1.04	8.28	1,1,1,1,1,18
Tol 1004-296SE	5.0e-13	0.30	52	2.69	69	1.08	8.20	1,1,1,1,1,18
Tol 1008-286	5.1e-14	1.05	123	9.55	395	1.30	8.17	1,1,1,21,1,21,4
CTS 1011	6.2e-14	0.34	93	3.80	233	1.28	8.18	1,1,1,1,1,18
CTS 1012	6.3e-14	0.01	204	1.40	8.41	3,3,-,-,22,22,3
CTS 1013	1.7e-14	0.00	38	3.40	185	1.29	8.08	1,1,1,1,1,18
Tol 1025-285	4.0e-14	0.79	9	0.31	27	1.40	8.71	1,1,1,2,1,22,17
Haro 24	4.8e-14	0.57	11	0.88	27	1.40	8.23	1,1,1,1,1,22,17
CTS 1014	2.2e-14	0.01	204	1.40	7.98	3,3,-,-,22,22,3
CTS 1016	1.7e-14	0.19	26	1.24	27	1.40	8.36	1,1,1,1,1,22,3
CTS 1017	2.2e-14	0.22	161	6.68	247	1.46	7.98	1,1,1,1,1,18
CTS 1018	1.8e-14	0.16	58	2.43	140	1.40	7.97	1,1,1,1,1,18
CTS 1019	4.2e-14	0.22	90	3.87	27	1.11	8.22	1,1,1,1,1,18
CTS 1020	1.5e-13	0.33	109	2.94	101	1.12	8.25	1,1,1,1,1,18
CTS 1022	2.6e-14	0.43	57	1.53	147	1.33	8.09	1,1,1,1,1,18
[F80] 30	2.9e-13	0.00	97	5.07	215	1.41	7.99	1,1,1,7,1,7,7
MRK 36	1.5e-13	0.08	62	3.48	96	1.38	7.89	1,1,1,1,1,18
UM 439	1.2e-13	0.05	49	4.30	27	1.39	8.01	1,1,1,1,1,18
UM 448	7.3e-13	0.40	48	1.16	151	1.08	8.17	1,1,1,1,1,18
Tol 1147-283	5.6e-14	0.20	40	1.08	79	1.51	7.88	1,1,1,1,1,18

Table 3
(Continued)

Galaxy	$F_{H\alpha}$ (erg s ⁻¹ cm ⁻²)	$C_{H\beta}$	$W_{H\beta}$ (Å)	[O III]/[O II]	N_e (cm ⁻³)	T_e (10 ⁴ K)	12+ log(O/H)	Ref.
UM 455	2.0e-14	0.48	29	4.32	27	1.73	7.74	1,1,1,1,1,1,18
UM 456	8.9e-14	0.06	44	3.09	27	1.41	7.95	1,1,1,1,1,1,18
UM 461	1.1e-13	0.05	155	9.43	115	1.66	7.77	1,1,1,1,1,1,18
UM 463	3.3e-14	0.17	74	6.08	102	1.32	7.92	1,1,1,20,1,11,11
CTS 1026	1.0e-12	0.33	204	1.40	8.30	3,3,-,-,22,22,3
UM 477	2.6e-13	0.88	17	0.34	979	1.40	9.12	1,1,1,1,1,22,16
UM 483	4.7e-14	0.45	19	0.84	133	1.71	7.85	1,1,1,11,1,11,11
CTS 1027	1.5e-13	0.08	50	1.88	63	1.01	8.35	8,8,8,8,8,8,8
MRK 1318	2.2e-13	0.27	68	1.70	78	1.01	8.27	1,1,1,1,1,1,18
CTS 1028	4.5e-14	0.57	82	3.90	344	1.40	8.05	1,1,1,1,1,1,18
UM 499	6.1e-13	0.55	24	0.45	611	1.40	8.82	1,1,1,1,1,22,16
Tol 1223-359	7.5e-14	0.16	129	7.18	27	1.73	7.54	1,1,1,12,1,12,12
Haro 30	6.1e-14	0.00	28	0.93	103	1.54	7.67	1,1,1,1,1,1,18
[SC98] 01	1.8e-14	0.14	34	1.39	45	1.40	8.27	1,1,1,1,1,22,17
CTS 1029	1.9e-14	0.29	35	1.05	489	1.40	8.42	1,1,1,1,1,22,3
[SC98] 11	204	1.40	...	-,-,-,-,22,22,-
UM 559	5.0e-14	0.00	535	4.92	204	1.58	7.72	1,1,1,1,22,9,9
[SC98] 68	2.1e-14	0.52	22	0.76	343	1.40	8.49	1,1,1,1,1,22,17
UM 570	3.1e-14	0.00	180	43.00	204	1.83	7.71	1,1,1,9,22,9,9
[SC98] 88	1.9e-14	0.29	20	1.24	339	1.41	8.02	1,1,1,1,1,1,18
CTS 1030	7.0e-14	0.01	204	1.40	8.25	3,3,-,-,22,22,3
POX 186	7.2e-14	0.01	274	19.26	342	1.66	7.74	1,1,1,1,1,1,18
CTS 1031	3.4e-14	0.22	204	1.40	8.23	3,3,-,-,22,22,3
Tol 1345-420	8.7e-14	0.27	51	2.89	71	1.07	8.26	1,1,1,1,1,1,18
CTS 1033	7.4e-14	0.24	59	8.69	155	1.42	8.01	1,1,1,1,1,1,18
Tol 1400-397	2.3e-14	0.20	204	1.40	...	2,2,-,-,22,22,-
UM 649	1.2e-14	0.00	204	1.40	...	2,2,-,-,22,22,-
CTS 1034	1.3e-14	0.28	20	1.53	1288	1.47	7.96	1,1,1,1,1,1,18
II ZW 70	2.7e-13	0.30	49	1.90	96	1.21	8.07	5,13,10,10,13,13,4
CTS 1035	1.5e-14	0.12	62	2.91	510	1.40	8.01	1,1,1,1,1,22,3
CTS 1037	4.0e-13	0.29	204	1.40	8.21	3,3,-,-,22,22,3
Cam 1543+0907	5.9e-14	0.05	192	8.96	74	1.68	7.71	1,1,1,1,1,1,18
Tol 1924-416	1.0e-12	0.11	100	4.86	131	1.35	8.01	1,1,1,1,1,1,18
Tol 1939-419	1.3e-14	0.00	204	1.40	...	2,2,-,-,22,22,-
Tol 1937-423	2.0e-14	0.70	5	0.49	39	1.40	8.48	1,1,1,1,1,22,17
CTS 1038	1.9e-13	0.53	204	1.40	7.82	3,3,-,-,22,22,3
CTS 1039	9.7e-14	0.01	204	1.40	7.70	3,3,-,-,22,22,3
Tol 2010-382	8.2e-14	0.76	204	1.40	...	14,2,-,-,22,22,-
Tol 2019-405	1.5e-14	0.10	11	1.90	76	1.45	7.99	1,1,1,1,1,1,18
Tol 2041-394	1.9e-14	0.00	204	1.40	...	2,2,-,-,22,22,-
NGC 6970	9.7e-14	0.00	204	1.40	...	14,2,-,-,22,22,-
MBG 20533-4410	1.0e-13	0.81	8	0.20	90	1.40	8.88	1,1,1,1,1,22,16
Tol 2122-408	2.6e-14	0.41	14	4.47	97	1.40	8.49	1,1,1,1,1,22,16
Tol 2138-405	8.9e-14	0.19	208	7.08	204	1.38	7.98	9,9,9,9,22,9,9
Tol 2138-397	1.8e-14	0.12	33	2.49	27	1.86	7.64	1,1,1,1,1,1,18
Tol 2146-391	2.8e-14	0.09	246	7.70	47	1.59	7.78	1,1,1,1,1,1,18
MBG 21567-1645	3.2e-14	1.36	2	0.08	281	1.40	8.93	1,1,1,1,1,22,17
MBG 22012-1550	3.9e-14	0.84	7	0.70	27	1.40	8.20	1,1,1,1,1,22,16
IC 5154	4.9e-14	0.38	10	0.79	250	1.40	8.52	1,1,1,1,1,22,17
ESO 533-G 014	5.7e-14	0.45	6	0.41	27	1.51	7.90	1,1,1,1,1,1,18
MCG -01-57-017	6.5e-14	0.10	11	0.23	27	1.40	8.37	1,1,1,1,1,22,16
Tol 2240-384	3.4e-14	0.37	165	8.72	204	1.53	7.85	1,1,1,1,22,1,18
MBG 23121-3807	2.4e-14	0.71	4	0.11	27	1.40	8.75	1,1,1,1,1,22,17
Tol 2326-405	4.1e-14	0.22	204	1.40	8.03	2,2,-,-,22,22,19
UM 167	1.2e-12	0.26	204	1.40	...	14,2,-,-,22,22,-
UM 191	3.6e-14	0.43	7	0.26	108	1.40	8.30	1,1,1,1,1,22,16

References. (1) Kehrig et al. 2004; (2) T91; (3) Pena et al. 1991; (4) Denicoló et al. 2002; (5) Telles et al. 2001; (6) Kniazev et al. 2001; (7) Izotov & Thuan 1998; (8) Vílchez & Iglesias-Páramo 2003; (9) Papaderos et al. 2006; (10) Mas-Hesse & Kunth 1999; (11) Kniazev et al. 2004; (12) Izotov et al. 2001; (13) Kehrig et al. 2008; (14) Coudé spectrophotometry; (15) Pustilnik et al. 2002; (16) O/H derived from p -method (Pilyugin 2000); (17) O/H derived from N2 calibrator (Denicoló et al. 2002); (18) O/H derived from T_e -method; (19) Melnick et al. 1988; (20) Masegosa et al. 1994; (21) Campbell et al. 1986; (22) mean values for T_e and N_e .

Table 4Errors in σ as a Function of Signal-to-Noise Ratio of the Line Emission

S/N H Lines	$\delta\sigma_{\text{H}}$ (km s ⁻¹)	S/N O Lines	$\delta\sigma_{\text{O}}$ (km s ⁻¹)
FEROS			
S/N < 10	2.9	S/N < 10	2.1
10 < S/N < 20	2.2	10 < S/N < 20	1.4
20 < S/N < 30	1.8	20 < S/N < 30	0.9
30 < S/N < 40	1.2	30 < S/N < 50	0.7
40 < S/N < 75	0.7	50 < S/N < 150	0.5
S/N > 75	0.4	S/N > 150	0.2
Coudé			
S/N < 110	4.6		
S/N > 110	3.5		

smaller than the theoretical value 2.87, we calculated $C_{\text{H}\beta}$ using the ratio $\text{H}\gamma/\text{H}\beta$. When the ratios were $\text{H}\alpha/\text{H}\beta < 2.87$ and $\text{H}\gamma/\text{H}\beta > 0.466$ simultaneously we adopted the zero value for $C_{\text{H}\beta}$. Dereddened fluxes I_{λ} were thus calculated by

$$I_{\lambda} = F_{\lambda} \exp[C_{\text{H}\beta}(1 + f_{\lambda})],$$

where F_{λ} is the published flux corrected by atmospheric extinction and f_{λ} is the interstellar reddening function normalized at $\text{H}\beta$. We adopted f_{λ} from Whitford (1958) as normalized by Lequeux et al. (1979).

$\text{H}\beta$ equivalent widths ($W_{\text{H}\beta}$) were taken directly from KTC for 91 objects. From the same work, ionization ratios, $[\text{O III}]\lambda\lambda 4959+5007/[\text{O II}]\lambda 3727$ (hereafter $[\text{O III}]/[\text{O II}]$) were directly determined for 80 objects from dereddened fluxes of oxygen lines.

We derived oxygen abundances for 51 objects adopting the T_e -method and the standard model for a two-zone photoionized H II region. This number was limited by the number of objects with all oxygen lines available in KTC, i.e., $[\text{O III}]\lambda\lambda 4959, 5007, [\text{O III}]\lambda 4363$, and $[\text{O II}]\lambda 3727$ lines. We did not consider those galaxies in which $[\text{O II}]\lambda 3727$ fluxes were indirectly determined by KTC. Temperatures for low- and high-ionization zones were derived according to Pagel et al. (1992) using the $[\text{O III}](\lambda\lambda 4959 + 5007)/\lambda 4363$ ratio and electron densities, $N_e(\text{S II})$. $N_e(\text{S II})$ was derived for 87 galaxies from the $[\text{S II}]\lambda 6717/\lambda 6731$ ratio, using TEMDEN from the NEBULAR package of IRAF, based on five-level atom calculations developed by Shaw & Dufour (1995). All $[\text{S II}]\lambda 6717/\lambda 6731$ ratios higher than 1.4 were fixed at this value, corresponding to a minimum $N_e(\text{S II})$ of 27 cm⁻³ in the TEMDEN task. For those galaxies where N_e was not directly determined or found in the literature, we assumed a mean value of 204 cm⁻³. Oxygen ionic abundances could be derived using Pagel et al. (1992) expressions for $\text{O}^{++}/\text{H}^{+}$ and $\text{O}^{+}/\text{H}^{+}$ to obtain the total oxygen abundance:

$$\frac{\text{O}}{\text{H}} = \frac{\text{O}^{+}}{\text{H}^{+}} + \frac{\text{O}^{++}}{\text{H}^{+}}.$$

Typical errors in oxygen abundances derived by the T_e -method and provided by Monte Carlo simulations were $\delta(\text{O}/\text{H}) = 0.05\text{--}0.06$.

For galaxies in KTC that could not have their abundances determined from the T_e -method, or were not even present in that sample, we compiled some recent results found in the literature (Kehrig et al. 2004) also using the T_e -method. The values for $W_{\text{H}\beta}$, $[\text{O III}]/[\text{O II}]$, $N_e(\text{S II})$, and $T_e(\text{O III})$ were also taken from most of these other works. For those galaxies where we could

not find oxygen abundances determined from the T_e -method, mainly due to the absence of the auroral $[\text{O III}]\lambda 4363$ line, we derived O/H empirically using the p -method (Pilyugin 2000) and N2 calibrator (Denicoló et al. 2002).

First, we calculated both high- and low-abundance values for O/H (Pilyugin 2000, Equations (4) and (6)). We only considered those values in agreement with the respective abundance regimes of the Pilyugin best fits, i.e., $12+\log(\text{O}/\text{H})_{P3} < 7.95$ or $12+\log(\text{O}/\text{H})_{P2} > 8.15$. In order to break the degeneracy when the values were acceptable, we adopted a criterion similar to the one described in van Zee et al. (1998). Those galaxies with $\log[\text{N II}](\lambda\lambda 6548 + 6584)/[\text{O II}](\lambda 3727 \text{ blended}) > -0.8$ should have high-abundance values assigned (P2), whereas those with $\log[\text{N II}]/[\text{O II}] < -1.05$ should have low-abundance values assigned (P3). With this criterion, we assigned 14 empirical abundance values for $12+\log(\text{O}/\text{H})$, all from the high-abundance side. Instead of using the calibrator $[\text{N II}]/\text{H}\alpha$ provided in van Zee et al. (1998) for the turnover region when the Pilyugin values were not calculated or acceptable, we used the N2 calibrator from Denicoló et al. (2002),

$$12 + \log(\text{O}/\text{H}) = 9.12 + 0.73 \times \text{N2},$$

where N2 is defined as $\text{N2} = \log([\text{N II}]\lambda 6584/\text{H}\alpha)$. For this, we also used $[\text{N II}]$ dereddened fluxes from KTC. The other 15 O/H ratios were calculated by the N2 calibrator. The uncertainties in oxygen abundances derived by both empirical methods (p -method and N2) were estimated to be $\delta(\text{O}/\text{H}) = 0.14$, corresponding to the rms of least-squares fits between T_e -method abundances and empirical abundances derived independently.

Table 3 presents all physical parameters discussed in this section. Columns 1–5 show the galaxy name, the observed flux of $\text{H}\alpha$ ($F_{\text{H}\alpha}$), the derived logarithmic reddening parameter ($C_{\text{H}\beta}$), the equivalent width of $\text{H}\beta$ ($W_{\text{H}\beta}$), the ionization ratio $[\text{O III}]/[\text{O II}]$, the derived electron density (N_e) and temperature (T_e), and oxygen abundance (O/H), and finally, the last column shows the references to the sources of the data in the same order in which they appear in the table.

3.3. Distance and $\text{H}\alpha$ Luminosity

The distances (D) to all galaxies in Mpc were derived using Hubble's law, $D = cz_{\text{H}}/H_0$, where z_{H} is the cosmological redshift of the galaxies and H_0 is the Hubble constant in km s⁻¹ Mpc⁻¹. Heliocentric redshifts (z_{hel}) were derived from the observed redshift ($z_{\text{obs}} = \Delta\lambda/\lambda$) by removing Earth's rotational and orbital motions using the resultant velocity component from the RVCORRECT routine of IRAF. This correction is smaller than 30 km s⁻¹ in modulus and it was only applied to the redshifts from FEROS spectra. An uncertainty of $\delta z_{\text{hel}} = 5 \times 10^{-5}$ was estimated for FEROS spectra redshifts and $\delta z_{\text{hel}} = 1.5 \times 10^{-4}$ for Coudé spectra redshifts. Heliocentric redshifts from FEROS were given priority over those from Coudé to derive distances for those galaxies observed with both instruments. We found z_{H} from z_{hel} by removing the solar motion with respect to the 3 K cosmic microwave background. We used the NASA/IPAC Extragalactic Database³ to obtain the resultant velocity correction (heliocentric to 3 K background) for all galaxies of our sample. Heliocentric redshifts and distances for all galaxies are presented in Columns 2 and 3 of Table 2.

³ <http://nedwww.ipac.caltech.edu/>

Table 5
Velocity Dispersion and H α Luminosities

Galaxy	σ (km s $^{-1}$)					log L (erg s $^{-1}$)
	FEROS				Coudé	
	H β	λ 4959	λ 5007	H α	H α	
UM 238	18.3 \pm 1.8	19.2 \pm 0.5	19.3 \pm 0.5	18.6 \pm 0.4	...	40.02
MBG 00463-0239	57.7 \pm 3.5	40.67
UM 304	78.2 \pm 2.2	89.8 \pm 2.1	86.1 \pm 1.4	78.2 \pm 0.4	76.3 \pm 4.6	41.55
Tol 0104-388	47.6 \pm 1.8	47.0 \pm 0.7	49.3 \pm 0.5	48.2 \pm 0.4	...	40.81
UM 306	19.1 \pm 1.2	17.4 \pm 0.5	18.1 \pm 0.5	19.1 \pm 0.4	...	40.25
UM 307	49.4 \pm 3.5	41.20
UM 323	18.9 \pm 2.2	21.4 \pm 0.9	19.5 \pm 0.5	18.0 \pm 0.4	...	39.78
Tol 0127-397	37.2 \pm 0.7	35.6 \pm 0.5	35.8 \pm 0.5	35.4 \pm 0.4	33.2 \pm 3.5	40.72
Tol 0140-420	28.6 \pm 2.2	27.2 \pm 2.1	27.2 \pm 2.1	26.4 \pm 0.4	...	40.35
UM 137	16.7 \pm 2.1	14.5 \pm 2.2	...	39.13
UM 151	28.7 \pm 2.9	22.2 \pm 2.1	26.4 \pm 2.1	31.6 \pm 1.8	...	40.39
UM 382	17.2 \pm 2.9	19.2 \pm 2.1	18.2 \pm 1.4	15.4 \pm 2.2	...	39.83
MBG 01578-6806	24.8 \pm 4.6	...
UM 391	57.7 \pm 2.2	...	79.3 \pm 1.4	59.1 \pm 0.4	59.6 \pm 4.6	41.00
UM 395	30.1 \pm 2.2	32.0 \pm 2.1	29.8 \pm 1.4	30.3 \pm 0.4	...	40.52
UM 396	27.1 \pm 2.2	27.4 \pm 0.2	27.4 \pm 0.5	26.7 \pm 0.4	...	40.49
UM 408	19.5 \pm 1.2	16.4 \pm 0.5	16.7 \pm 0.5	19.3 \pm 0.4	...	39.73
UM 417	12.1 \pm 2.9	13.4 \pm 2.1	14.8 \pm 0.7	15.3 \pm 1.2	...	39.18
Tol 0226-390	89.9 \pm 0.7	83.5 \pm 0.5	81.1 \pm 0.2	...	75.5 \pm 3.5	41.89
CTS 1003	24.7 \pm 1.8	25.1 \pm 0.5	24.7 \pm 0.7	25.2 \pm 0.4	...	40.10
MBG 02411-1457	33.7 \pm 4.6	40.09
Tol 0242-387	98.2 \pm 2.9	113.1 \pm 2.1	111.7 \pm 0.9	96.9 \pm 2.9	...	43.11
CTS 1004	43.8 \pm 2.9	43.5 \pm 2.1	44.3 \pm 0.2	41.21
CTS 1005	49.4 \pm 1.8	46.8 \pm 2.1	46.3 \pm 0.5	48.6 \pm 0.4	...	41.81
Tol 0440-381	34.3 \pm 0.7	32.0 \pm 0.5	31.8 \pm 0.2	34.7 \pm 0.4	47.4 \pm 4.6	41.36
CTS 1006	36.7 \pm 0.4	33.5 \pm 0.2	33.7 \pm 0.2	37.0 \pm 0.4	...	41.22
CTS 1007	29.5 \pm 1.8	27.4 \pm 0.5	26.8 \pm 0.5	28.5 \pm 0.4	...	41.20
CTS 1008	49.0 \pm 1.8	45.6 \pm 0.5	45.6 \pm 0.7	48.0 \pm 1.2	...	41.81
Tol 0505-387	21.8 \pm 2.9	19.9 \pm 2.1	22.1 \pm 0.7	21.0 \pm 1.8	...	40.55
Tol 0510-400	34.0 \pm 1.8	31.4 \pm 0.9	31.1 \pm 0.9	31.4 \pm 0.7	...	41.21
Tol 0528-383	18.0 \pm 2.2	18.9 \pm 0.9	19.6 \pm 1.4	19.5 \pm 0.7	...	40.27
II ZW 40	32.9 \pm 0.4	32.5 \pm 0.2	32.8 \pm 0.2	33.5 \pm 0.4	31.8 \pm 3.5	40.17
Tol 0559-393	50.7 \pm 2.2	41.9 \pm 2.1	46.8 \pm 0.7	48.3 \pm 1.2	...	41.53
Tol 0610-387	16.6 \pm 2.9	...	23.2 \pm 0.7	20.1 \pm 0.7	...	39.55
Tol 0614-375	44.8 \pm 1.8	50.8 \pm 2.1	50.0 \pm 0.9	48.4 \pm 0.4	...	42.01
Tol 0633-415	32.0 \pm 0.7	30.7 \pm 0.5	31.1 \pm 0.2	30.6 \pm 0.4	...	41.09
Tol 0645-376	28.7 \pm 2.2	30.5 \pm 0.9	29.4 \pm 0.5	29.6 \pm 0.7	23.3 \pm 3.5	40.76
MRK 1201	46.0 \pm 2.2	46.0 \pm 0.7	...	40.83
Cam 0840+1201	36.8 \pm 1.8	34.6 \pm 0.7	34.4 \pm 0.2	34.9 \pm 0.4	...	41.37
Cam 0840+1044	15.4 \pm 1.8	13.4 \pm 1.4	13.9 \pm 0.2	14.8 \pm 0.4	...	39.94
Cam 08-28A	51.0 \pm 2.2	43.7 \pm 1.4	44.7 \pm 0.5	42.14
MRK 710	56.2 \pm 1.8	...	53.7 \pm 1.4	51.0 \pm 0.4	47.8 \pm 3.5	40.89
MRK 711	94.0 \pm 0.7	86.0 \pm 0.7	87.2 \pm 0.5	95.3 \pm 0.4	...	41.59
Tol 0957-278	24.7 \pm 2.2	26.7 \pm 1.4	26.2 \pm 0.5	26.9 \pm 0.4	22.0 \pm 3.5	40.05
Tol 1004-296NW	31.9 \pm 3.5	40.83
Tol 1004-296SE	27.1 \pm 3.5	40.57
Tol 1008-286	24.9 \pm 0.4	25.3 \pm 0.2	25.0 \pm 0.2	25.5 \pm 0.4	...	41.08
CTS 1011	21.2 \pm 0.7	20.6 \pm 0.5	20.7 \pm 0.5	21.1 \pm 0.4	...	40.59
CTS 1012	17.0 \pm 0.7	16.1 \pm 0.5	15.8 \pm 0.2	16.6 \pm 0.4	...	40.29
CTS 1013	33.7 \pm 2.9	33.5 \pm 1.4	34.0 \pm 0.5	31.6 \pm 1.8	...	40.45
Tol 1025-285	58.8 \pm 2.9	...	60.0 \pm 1.4	55.0 \pm 1.2	...	41.47
Haro 24	43.0 \pm 2.2	38.9 \pm 1.4	42.7 \pm 0.7	46.3 \pm 0.7	...	41.69
CTS 1014	56.6 \pm 2.2	42.9 \pm 0.9	44.2 \pm 0.7	50.0 \pm 1.8	...	41.23
CTS 1016	35.1 \pm 2.9	32.6 \pm 2.1	34.5 \pm 1.4	39.7 \pm 1.8	...	40.79
CTS 1017	27.7 \pm 2.2	28.9 \pm 0.7	28.6 \pm 1.4	27.5 \pm 0.7	...	40.94
CTS 1018	34.8 \pm 1.8	32.2 \pm 0.5	32.0 \pm 0.5	35.1 \pm 0.7	...	40.91
CTS 1019	45.2 \pm 2.9	45.5 \pm 0.7	46.0 \pm 0.5	49.1 \pm 0.7	...	41.76
CTS 1020	34.5 \pm 0.4	34.4 \pm 0.5	35.0 \pm 0.2	35.1 \pm 0.4	...	40.98
CTS 1022	22.6 \pm 1.8	20.9 \pm 0.7	21.1 \pm 0.7	24.9 \pm 0.4	...	40.37
[F80] 30	20.6 \pm 0.4	18.6 \pm 0.2	18.6 \pm 0.2	20.2 \pm 0.4	...	40.07
MRK 36	17.1 \pm 1.2	17.2 \pm 0.5	17.8 \pm 0.2	16.8 \pm 0.4	...	39.55
UM 439	17.7 \pm 0.4	17.7 \pm 0.2	17.6 \pm 0.2	18.0 \pm 0.4	18.9 \pm 4.6	39.86
UM 448	75.1 \pm 0.7	76.6 \pm 0.7	75.3 \pm 0.5	78.3 \pm 0.4	61.2 \pm 3.5	42.04

Table 5
(Continued)

Galaxy	σ (km s ⁻¹)					log L (erg s ⁻¹)
	FEROS				Coudé	
	H β	$\lambda 4959$	$\lambda 5007$	H α	H α	
Tol 1147-283	17.0 \pm 2.2	20.0 \pm 0.9	17.9 \pm 0.5	17.8 \pm 0.4	...	39.95
UM 455	22.6 \pm 2.2	18.5 \pm 0.7	18.2 \pm 0.9	26.2 \pm 1.2	...	40.25
UM 456	16.1 \pm 0.7	15.7 \pm 0.5	15.8 \pm 0.2	15.9 \pm 0.4	...	40.00
UM 461	12.5 \pm 0.4	12.5 \pm 0.2	12.6 \pm 0.2	12.5 \pm 0.4	...	39.77
UM 463	19.2 \pm 2.2	17.0 \pm 0.9	16.7 \pm 0.2	17.0 \pm 0.7	...	39.50
CTS 1026	43.1 \pm 0.4	43.0 \pm 0.2	42.9 \pm 0.2	42.5 \pm 0.4	...	41.02
UM 477	57.4 \pm 1.2	...	72.3 \pm 1.4	57.2 \pm 0.4	55.0 \pm 3.5	40.80
UM 483	17.2 \pm 0.7	19.4 \pm 0.5	18.4 \pm 0.2	17.1 \pm 0.4	...	40.22
CTS 1027	21.0 \pm 0.4	20.1 \pm 0.5	20.5 \pm 0.2	21.2 \pm 0.4	...	40.29
MRK 1318	17.1 \pm 1.2	17.0 \pm 0.5	17.2 \pm 0.2	17.7 \pm 0.4	19.8 \pm 4.6	40.44
CTS 1028	27.1 \pm 1.2	26.8 \pm 0.5	27.2 \pm 0.5	26.6 \pm 0.4	...	40.92
UM 499	44.0 \pm 3.5	41.31
Tol 1223-359	17.5 \pm 2.2	16.9 \pm 0.9	17.4 \pm 0.2	18.4 \pm 0.4	...	40.35
Haro 30	43.4 \pm 2.2	47.6 \pm 2.1	46.0 \pm 0.9	44.8 \pm 0.7	...	40.55
[SC98] 01	22.6 \pm 2.9	19.8 \pm 1.4	17.7 \pm 0.7	19.6 \pm 0.7	...	39.80
CTS 1029	31.4 \pm 1.8	...	40.94
[SC98] 11	31.5 \pm 1.8	31.8 \pm 0.9	30.5 \pm 0.5	31.9 \pm 0.4
UM 559	16.9 \pm 0.7	16.9 \pm 0.5	17.0 \pm 0.2	17.5 \pm 0.4	...	39.48
[SC98] 68	30.6 \pm 2.9	33.6 \pm 2.1	32.1 \pm 0.9	31.3 \pm 0.7	...	40.79
UM 570	20.1 \pm 2.2	21.8 \pm 0.9	21.2 \pm 0.5	20.8 \pm 0.4	...	40.57
[SC98] 88	25.1 \pm 2.2	22.4 \pm 1.4	21.2 \pm 1.4	26.1 \pm 1.2	...	40.19
CTS 1030	29.4 \pm 0.4	30.5 \pm 0.5	30.1 \pm 0.2	29.7 \pm 0.4	...	40.59
POX 186	14.1 \pm 0.7	14.4 \pm 0.5	14.3 \pm 0.2	14.4 \pm 0.4	...	39.62
CTS 1031	31.6 \pm 2.2	31.6 \pm 1.4	33.5 \pm 0.7	30.8 \pm 0.4	...	41.19
Tol 1345-420	20.4 \pm 2.2	18.6 \pm 0.7	19.6 \pm 0.2	20.4 \pm 0.4	24.9 \pm 4.6	40.35
CTS 1033	48.2 \pm 0.4	48.8 \pm 0.2	48.4 \pm 0.2	48.3 \pm 0.4	...	40.79
Tol 1400-397	32.4 \pm 2.2	32.1 \pm 1.4	33.5 \pm 0.5	34.3 \pm 0.7	...	40.84
UM 649	27.1 \pm 2.2	23.1 \pm 1.4	25.0 \pm 0.5	25.5 \pm 1.8	...	40.27
CTS 1034	...	27.1 \pm 2.1	25.5 \pm 1.4	26.6 \pm 1.8	...	40.38
II ZW 70	21.0 \pm 1.2	20.0 \pm 0.5	20.5 \pm 0.2	24.3 \pm 0.4	...	40.27
CTS 1035	27.4 \pm 2.9	27.7 \pm 2.1	26.6 \pm 0.5	23.9 \pm 2.2	...	40.53
CTS 1037	38.4 \pm 0.4	38.3 \pm 0.2	37.5 \pm 0.2	37.7 \pm 0.4	...	41.61
Cam 1543+0907	30.2 \pm 0.4	29.1 \pm 0.2	28.6 \pm 0.2	29.5 \pm 0.4	...	41.29
Tol 1924-416	35.4 \pm 3.5	41.34
Tol 1939-419	23.6 \pm 0.9	22.5 \pm 1.2	...	40.22
Tol 1937-423	24.0 \pm 2.2	19.2 \pm 1.4	22.1 \pm 0.7	21.3 \pm 0.7	29.6 \pm 4.6	40.00
CTS 1038	...	51.8 \pm 2.1	51.6 \pm 0.7	41.98
CTS 1039	40.9 \pm 0.4	41.7 \pm 0.2	41.7 \pm 0.2	40.9 \pm 0.4	...	41.61
Tol 2010-382	37.0 \pm 1.8	...	36.7 \pm 1.4	34.2 \pm 0.4	37.0 \pm 3.5	41.34
Tol 2019-405	25.8 \pm 1.8	24.5 \pm 0.5	24.7 \pm 0.7	21.9 \pm 0.4	...	39.89
Tol 2041-394	...	29.3 \pm 2.1	27.5 \pm 0.7	28.5 \pm 1.8	...	40.41
NGC 6970	46.0 \pm 4.6	40.77
MBG 20533-4410	55.8 \pm 4.6	41.31
Tol 2122-408	26.4 \pm 1.8	26.4 \pm 0.7	26.6 \pm 0.5	24.5 \pm 0.4	25.6 \pm 4.6	40.32
Tol 2138-405	59.5 \pm 2.2	59.8 \pm 0.9	59.9 \pm 0.5	62.1 \pm 1.8	...	41.92
Tol 2138-397	22.2 \pm 2.2	24.9 \pm 1.4	22.2 \pm 0.7	23.1 \pm 0.7	...	40.01
Tol 2146-391	26.8 \pm 1.8	23.0 \pm 0.5	24.2 \pm 0.2	25.6 \pm 0.4	...	40.75
MBG 21567-1645	103.5 \pm 4.6	41.17
MBG 22012-1550	92.7 \pm 4.6	41.71
IC 5154	33.2 \pm 3.5	40.30
ESO 533-G 014	14.5 \pm 3.5	40.16
MCG -01-57-017	22.0 \pm 3.5	40.06
Tol 2240-384	49.3 \pm 2.2	50.3 \pm 0.7	51.8 \pm 0.2	51.6 \pm 0.4	...	41.85
MBG 23121-3807	27.3 \pm 4.6	40.04
Tol 2326-405	37.3 \pm 0.7	43.7 \pm 2.2	...	41.56
UM 167	73.2 \pm 3.5	41.39
UM 191	30.3 \pm 2.2	...	39.2 \pm 0.9	32.0 \pm 0.4	33.3 \pm 3.5	40.90

H α luminosities ($L_{H\alpha}$) were therefore derived from dereddened fluxes ($I_{H\alpha}$) and D ($L_{H\alpha} = 4\pi D^2 I_{H\alpha}$). We have used H α rather than H β in the L - σ relation since it is more intense and

relatively less affected by extinction and underlying absorption. The last column of Table 5 shows the derived H α luminosities for 118 galaxies for which we had reliable spectrophotometry.

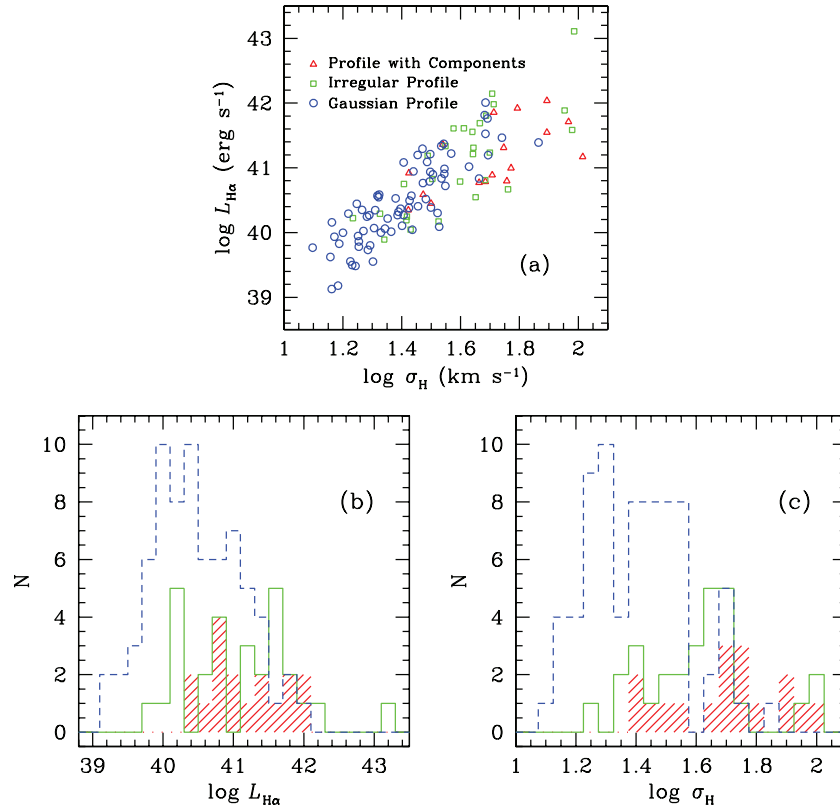


Figure 6. (a) $L_{H\alpha}$ – σ_H for 117 galaxies with obtained spectrophotometry, (b) luminosity distribution, and (c) velocity dispersion distribution. The color codes for each class of galaxy (G, I, and C) are as given in the label of plot (a).

(A color version of this figure is available in the online journal.)

The error in luminosity is very difficult to evaluate precisely since it depends on several factors. First, slit spectrophotometry for extended objects suffers intrinsically from the aperture effect (see Section 4.1). In addition, individual spectrophotometric errors were not provided by KTC; instead, they provided the random error of the flux measurements of the line emissions as being in the range 5%–40% for $F > 10^{-15}$ erg s⁻¹ cm⁻², decreasing for high intensity lines. However, they compared their results with those in T91 showing good agreement with their spectrophotometry. A point in favor of these new spectrophotometric data is their homogeneity in technique and instrumentation. In view of this, to obtain quantitative results in the analysis sections, we will consider only a sample of homogeneous spectrophotometric data, i.e., luminosities derived from KTC data and only a few newly available data derived using similar techniques.

3.4. The L – σ Relation

Figure 6(a) shows the L – σ relation in logarithmic units for 117 galaxies all observed with the FEROS and Coudé spectrographs. We also show the $L_{H\alpha}$ distribution in (b) and σ in (c) for each subsample of line profile class (G, I, and C), which will aid in the visualization of the subsample properties highlighted below. In Figure 6(a) we have plotted all galaxies for which we have obtained spectrophotometric data. This figure shows the strong correlation between the nebular luminosity and velocity dispersion and confirms, once more, the existence of this relation for H II Gs, but now for a sample of more than 100 galaxies, doubling the old samples studied in the past. Galaxies that present irregular profiles, especially those showing pro-

files with components, are systematically concentrated in the high velocity dispersion ($\log \sigma > 1.6$) and luminosity ($\log L_{H\alpha} > 41$) regions of the L – σ plot (top right). On the other hand, galaxies showing a Gaussian profile are more concentrated in the regime $\log \sigma < 1.6$ (bottom left), but for typical values of σ for single GHII Rs, they span from 12–30 km s⁻¹ ($1.1 < \log \sigma < 1.5$) to ~ 60 km s⁻¹ ($\log \sigma \sim 1.8$). It is clear in Figure 6(a) that galaxies showing irregularities and multiple components in their emission line profiles contribute to flattening of the L – σ relation resulting in its curved shape toward high L and σ values. This behavior was in fact predicted by MTM, but they identified only two galaxies that clearly deviate from the mean line (Tol 0226-390 and Tol 0242-387) due to their sample size. These two galaxies are also presented in our sample and were classified as I. MTM restricted their analysis to those objects that present $W_{H\beta} > 30$ Å. We will show below that this criterion also seems to be efficient for selecting galaxies with the most Gaussian line profiles.

In order to minimize the uncertainties due to a heterogeneous data set, we further analyze the L – σ relation for those galaxies that have line widths measured from FEROS data and spectrophotometry compiled from KTC’s work. An additional four objects (UM 382, CTS 1027, II Zw 70, and Tol 2138-405) that have good new spectrophotometry are also included.

Figure 7 shows the L – σ relation for the homogeneous sample described above including galaxies with close to Gaussian emission line profiles (81 objects). The regression fits for the total sample and for the G subsample only (53 objects) are presented in Table 6. The class of ordinary least-square (OLS) fits used in this work is appropriate for problems where the intrinsic scatter dominates the errors arising from

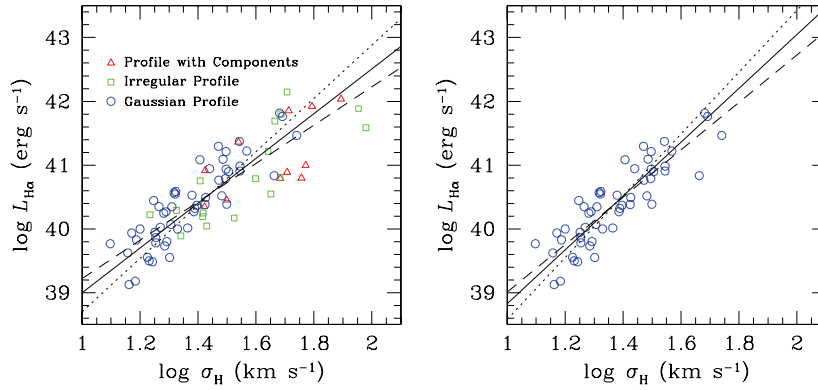


Figure 7. $L_{\text{H}\alpha}$ – σ_{H} relation for all galaxies with homogeneous spectrophotometry (81 objects G, I, and C, left) and for only those showing regular Gaussian profiles (53 objects G, right). The dashed line represents OLS(Y|X), the dotted line represents OLS(X|Y), and the solid line represents the bisector fit. All regression coefficients are presented in Table 6.

(A color version of this figure is available in the online journal.)

Table 6
Regressions for $\log L_{\text{H}\alpha}$ Versus $\log \sigma_{\text{H}}$

Linear Regression	Intercept (A)	Slope (B)	rms
All galaxies (81 objects)			
Pearson correlation coefficient (r) = 0.85, $\log L = A + B \times \log \sigma$			
OLS(Y X)	36.21 ± 0.32	3.01 ± 0.23	0.37
OLS(X Y)	34.52 ± 0.38	4.18 ± 0.27	
OLS Bisector	35.49 ± 0.32	3.51 ± 0.23	
Galaxies with Gaussian profiles (53 objects), $r = 0.88$			
OLS(Y X)	35.29 ± 0.42	3.72 ± 0.31	0.31
OLS(X Y)	33.73 ± 0.47	4.85 ± 0.34	
OLS Bisector	34.61 ± 0.41	4.22 ± 0.30	
More restrictive subsample (37 objects), $r = 0.90$			
OLS(Y X)	34.80 ± 0.41	4.14 ± 0.29	0.29
OLS(X Y)	33.45 ± 0.53	5.13 ± 0.38	
OLS Bisector	34.19 ± 0.43	4.58 ± 0.30	

the measurement process (Isobe et al. 1990). We argue that OLS(Y|X) is most appropriate for describing the L – σ relation for our data set and is best for comparison with previous calibrations (MTM; Telles et al. 2001). A second point is that the uncertainties in σ are much smaller than those in the luminosity, which justifies treating the first as an independent parameter in a direct linear regression. Nevertheless, the other fits give us an idea of the maximum limits of the regression coefficients (slope and zero point).

It is clear that the L – σ relation including only G galaxies is tighter and steeper than the one including the whole sample of HII Gs. This suggests that the Gaussianity of the emission line profiles in these systems may be associated with the nature of the L – σ relation. Figure 8 shows the $W_{\text{H}\beta}$ distribution for each class (G, I, and C). Note that most G galaxies are concentrated in the region of high $W_{\text{H}\beta}$ ($> 30 \text{ \AA}$). Thus, a sample selection criterion based on high $W_{\text{H}\beta}$ would also be efficient for selecting galaxies with the most Gaussian profiles. The consequences of this result regarding the nature of the L – σ relation are profound. Since $W_{\text{H}\beta}$ is an age indicator for the current starburst, resulting Gaussian line profiles may be associated with the youngest systems. If the L – σ relation for HII Gs has in fact an upper envelope described by those galaxies with zero age and maximum $W_{\text{H}\beta}$ values, it should be populated only by HII Gs showing the most Gaussian line profiles. In Section 4.2, we will be more rigorous in selecting a subsample of G galaxies with the most Gaussian line profiles by a semi-quantitative criterion in order to investigate if this

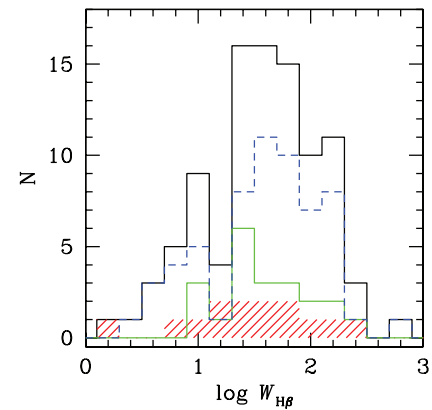


Figure 8. $\text{H}\beta$ equivalent width distributions (in log) for each class of galaxies, namely G (53), I (17), and C (11) presented in Figure 7. The solid line represents the distribution including all subsamples (81).

(A color version of this figure is available in the online journal.)

has additional consequences on the slope and scatter of the L – σ relation.

4. DATA ANALYSIS

4.1. Aperture Effects

The L – σ relation may be affected in principle by the aperture effect in two ways. First, if the observation comes from fixed-slit

spectroscopy ($\sim 2''$), as in this work, nearby objects should have underestimated fluxes and hence underestimated luminosities as well. Furthermore, extended and more compact objects, both at the same distance, may suffer differentially from this effect. This effect also may have implications for determining their physical conditions (Kewley et al. 2005). An aperture correction factor may be applied to our calibration by using the available data in Lagos et al. (2007). They observed a sample of HII Galaxies with H β narrowband imaging and analyzed the surface photometry as compared with the spectrophotometry of Kehrig et al. (2004). Many of the galaxies in their sample are also part of our present sample. Taking into account the observational and calibration errors in their analysis, there is a constant offset of the order of the observational scatter in the comparison that can be added to our derived L_{spec} : $\Delta L_{\text{H}\beta} \sim 0.25$ with an rms = 0.2, comparable to the rms of our L - σ relation. We have not done this a priori, since this correction would only introduce additional observational scatter, masking the contribution of the physical parameters in the analysis of the manifold of HII Galaxies. This effect is expected to be negligible for galaxies beyond >100 Mpc according to this analysis, and an improvement in this calibration will only come when this relation is verified for a sample of HII Galaxies beyond the local supercluster with new spectrophotometric data sets and new high-resolution spectroscopy. We have also verified that a correlation of the narrowband surface photometry of the main star-forming knot seems to be tighter than with the narrowband surface photometry of the integrated galaxy. This may be due to the mixed morphology of the galaxies as a function of luminosity (see Lagos et al. 2007; Telles et al. 1997), but also due to the very nature of the L - σ relation in the sense that it may be more closely related to the local gravitational potential of the starburst rather than the global dynamics. The relation still holds for the determination of galactic masses if we assume that more massive galaxies host more massive starbursts in a homologous way. These issues remain to be investigated in more detail.

Multiplicity of star-forming regions and the aperture effect can also introduce a bias in σ determination—a single observation integrates light from more than one starburst region in the same galaxy. This could introduce a systematic velocity component in the integrated line profiles since Super Star Clusters and their associated GHII Regions may present relative radial velocities that would add light in a non-trivial way. Although multiplicity does not necessarily preclude Gaussianity, it to be usually seems associated with asymmetric line profiles (Bordalo et al. 2009). We have also found very compact objects presenting line profiles with multiple components (e.g., CTS 1033 shown in Figure 9). However, most of the galaxies classified as C are not compact, but extended systems frequently associated with nuclear starburst galaxies, where the systemic rotational component dominates the features in emission line profiles.

The multiplicity effect seems to be inherent in the L - σ relation causing no strong bias, otherwise the L - σ relation would not be verified even in the short redshift range of our sample. The physical sizes covered by the observations span from a few hundred parsecs in nearby objects (e.g., UM 461 and MRK 36), characterizing sizes of single GHII Regions, to a few kiloparsecs (e.g., CTS 1008 and Cam 08-28A). In addition, multiplicity and aperture effects can be greatly reduced by selecting only the galaxies showing the most Gaussian line profiles.

4.2. Gaussian Profile Galaxies

In order to find a more homogeneous sample and, in addition, test the visual classification presented in Section 3.1, we have further adopted a semi-quantitative criterion to search for galaxies with the most Gaussian emission line profiles. These seem to be the ones that show lower scatter in the L - σ plane, as suggested in Figure 7, and therefore deserve special attention. The quantitative estimators that we used were the skewness (ξ) and kurtosis (κ) of the emission line profiles (see Miesch et al. 1999, for the use of these estimators in one-point velocity statistics of star-forming regions). These estimators are related to the third (m_3) and fourth (m_4) moments of the distribution through the formulae

$$\xi = \frac{m_3}{s^3}$$

and

$$\kappa = \frac{m_4}{s^4},$$

where s is the standard deviation of the distribution and m_3 and m_4 are their higher moments.⁴ For practical cases concerning real data spectra, where λ is the wavelength and y is the flux, the formulae for these estimators can be written as

$$\text{mean} = \mu = \frac{\sum \lambda \cdot y}{\sum y},$$

$$\text{standard deviation} = s = \sqrt{\frac{1}{\sum y} \sum (\lambda - \mu)^2 \cdot y},$$

$$\text{skewness} = \xi = \frac{1}{\sum y} \frac{\sum (\lambda - \mu)^3 \cdot y}{s^3},$$

$$\text{kurtosis} = \kappa = \frac{1}{\sum y} \frac{\sum (\lambda - \mu)^4 \cdot y}{s^4}.$$

Before we calculated the ξ and κ estimators, we smoothed all FEROS spectra with a box of 11 pixels (FEROS's scale is $0.03 \text{ \AA pixel}^{-1}$) using SPLOT. Since our aim was to estimate the global shape of the emission lines, the smooth procedure is very useful for eliminating high-frequency noise. The most Gaussian profile galaxies were selected as the ones which met the criterion of symmetry:⁵ $|\xi| < 0.1$ and $2.9 < \kappa < 3.1$. The estimators were calculated in a window centered at the mean, obtained from the single Gaussian fit (centroid), and defined as the one in which the line intensity falls to 20% of its peak value. This methodology ensures that the estimators show a good consistency between them, however, the size of the integration window over the λ interval is somewhat a matter of definition which should be based on the quality of the data.

Only FEROS galaxies with S/N in the line greater than 30 were analyzed using this method. Emission line profiles of 49 galaxies met the above criterion of symmetry. Two examples (UM463 and [F80] 30) are presented in Figure 9 (upper panels), including their shape estimators, ξ and κ . We also present the H α emission line profile of II Zw 40 ($\xi = 0.18$, $\kappa = 3.05$) as an example in which the criterion of symmetry was

⁴ We used s to denote the standard deviation so as not to confuse this with the velocity dispersion derived (σ).

⁵ $\xi = 0$ and $\kappa = 3$ for the Gaussian distribution.

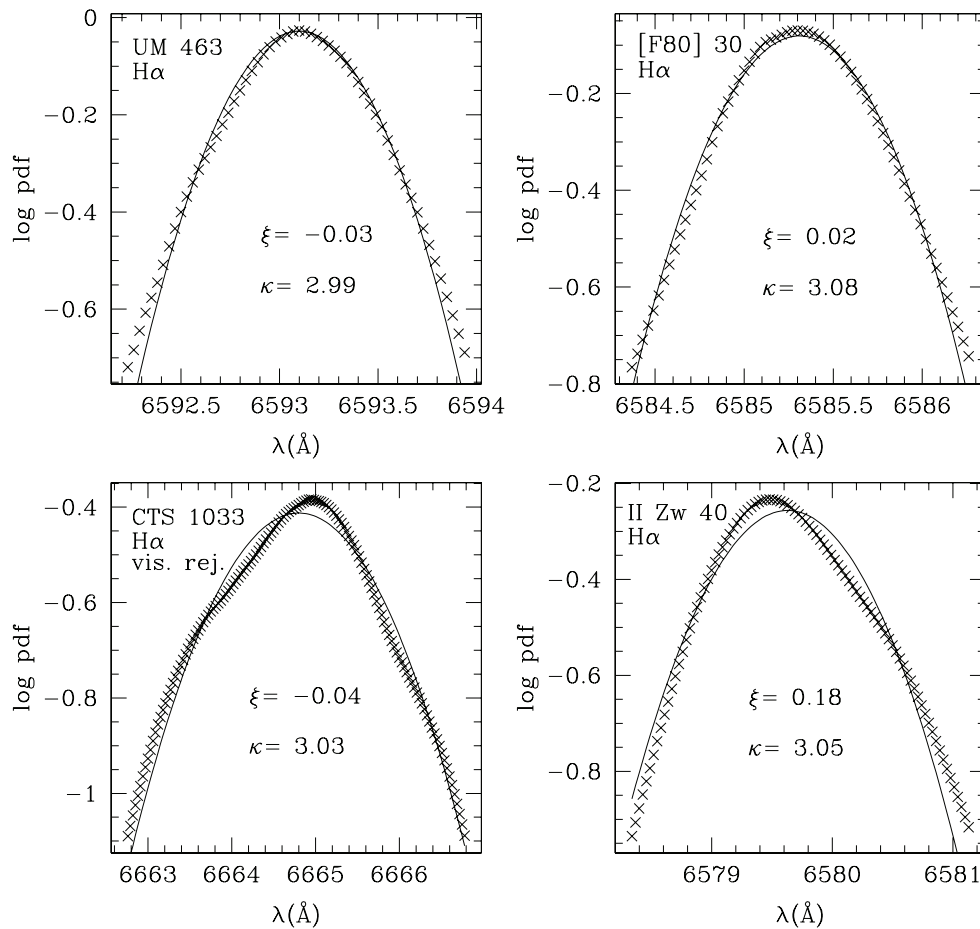


Figure 9. Examples of emission line profiles in linear-logarithmic axes. UM 463 (upper left) and [F80] 30 (upper right) met the criterion of symmetry described in the text (G') (bottom left), CTS 1033 was qualitatively visually rejected by presenting multiple components, and II Zw 40 (bottom right) does not meet the symmetry criterion. Measurements of ξ and κ estimators are shown in each panel. Solid lines represent single Gaussian fits to the observed profiles (crosses).

efficient to reject profiles with strong asymmetries (Figure 9, bottom right). Most estimators were calculated using the H α line and only a few were calculated using [O III] 5007 Å due to the presence of bad pixels or significantly lower S/N in H α . A comparison with the G subsample classified visually (Table 2) showed good agreement except for six galaxies that were previously classified as I or C, namely Tol 0104-388, Tol 0957-278, CTS 1030, CTS 1033, CTS 1037, and CTS 1039. These objects were thus visually rejected. We kept the visual classification for these galaxies since the first two objects present two intense components that are identified in the other emission lines observed, while CTS 1033 presents at least three emission components (Figure 9, bottom left). The last is a very special case in which asymmetries in the integration window are compensated for resulting in estimators that mimic a symmetric profile ($\xi = -0.04$, $\kappa = 3.03$). The other three objects present intense broad components not well evaluated in the integration window though they are symmetric. Thus, 43 galaxies compose a more restrictive subsample of the galaxies showing the most Gaussian line profiles and they were assigned type G' in Table 2.

The need for a qualitative analysis of the emission line profiles is in fact a limitation of the method applied to our data. Since the S/N is relatively low in the wings of the line, we need to limit the integration window to a fixed proportion of the peak value (see above) in order to maintain consistency between the values from very different S/N lines. Nevertheless, the method

provides a way to determine a homogeneous sample of galaxies based on their kinematic properties.⁶

Table 6 shows the regression fits for the L - σ relation considering the more restrictive subsample G'. From 43 objects identified as G', 37 had homogeneous observational data as described in Section 3.4 and were used to derive the calibration coefficients. Although this sample presents few objects in the range $1.6 < \log \sigma < 1.8$, the OLS fits show that the L - σ is steeper than the one for the whole G subsample (53 objects). We conclude that the galaxies showing the most Gaussian line profiles show a L - σ relation that could be identified as an upper envelope $L \propto \sigma^4$ with minimum scatter $\delta \log L_{H\alpha} = 0.29$.

4.3. The Second Parameter

Terlevich & Melnick (1981) and Melnick et al. (1988) have suggested that the dependent parameter L_{Balmer} can be predicted by σ and O/H, which should define the manifold of HII Gs. Telles & Terlevich (1993) also showed that the structural parameter, namely the radius of the burst should be considered a second parameter in L - σ , acting remarkably similarly to the effective radius in the fundamental plane of elliptical galaxies. It is crucial to investigate the existence of an independent second parameter (or a third) in the L - σ relation not only to obtain a precise distance indicator but also to understand the physics behind this scaling relation. If the underlying relation is in fact that between

⁶ Complete data from this analysis are available at <http://www.on.br/astro/etelles/lsigma>.

Table 7
Correlation Matrix for the PCA Analysis (95 Objects)

	$\log L_{H\alpha}$	$\log \sigma_H$	$\log (O/H)$	$\log W_{H\beta}$	$\log [O III]/[O II]$
$\log L_{H\alpha}$	1				
$\log \sigma_H$	0.82	1			
$\log (O/H)$	0.22	0.47	1		
$\log W_{H\beta}$	0.13	-0.15	-0.58	1	
$\log [O III]/[O II]$	-0.03	-0.32	-0.69	0.86	1

mass and luminosity, as proposed by these authors, then σ can be used properly to obtain dynamical masses of these systems with great relevance for the high-redshift studies of H II Gs counterparts, such as the Lyman break galaxies (Lowenthal et al. 2009, and references therein).

We have used principal component analysis (PCA) to investigate the relative dependence of the L - σ relation on a possible second parameter based on our new data set, following the early analysis by MTM. Let us first analyze the largest sample possible considering the five parameters (variables)— $L_{H\alpha}$, σ_H , O/H , $W_{H\beta}$, and $[O III]/[O II]$. The sample includes $n = 95$ objects with all these quantities known (Tables 3 and 5). All quantities were considered in logarithmic scales. Table 7 shows the lower triangle of the correlation matrix. Visual analysis of Table 7 shows that strong correlations are found between $W_{H\beta}$ and $[O III]/[O II]$ ($r = 0.86$) and $L_{H\alpha}$ and σ_H ($r = 0.82$). It is also worth noting that the correlations between $L_{H\alpha}$ and $[O III]/[O II]$, $L_{H\alpha}$ and $W_{H\beta}$, and σ_H and $W_{H\beta}$ are near zero. The correlations of O/H and $W_{H\beta}$ and O/H and $[O III]/[O II]$ are negative, while O/H and $L_{H\alpha}$ and O/H and σ_H are positive.

The first three principal components (PCs) with their loadings⁷ obtained from the correlation matrix as well as the eigenvalues (l) and the respective individual percentages ($l/5$) of total variance (5) are presented in Table 8. Nearly 88% of the variance among the 95 sample points lies in only two dimensions. The two dimensions of the manifold can easily be verified due to the bimodal behavior of the variance (Jolliffe 2002). The first two principal components (PCI and PCII) present eigenvalues well above 1 (or $1/5 = 20\%$), while the others lie well below this value. In addition, one can estimate the confidence interval for the eigenvalue 1 using the formula $\sqrt{2l^2/(n-1)}$ which provides $l = 1.00 \pm 0.15$ (or $20\% \pm 3\%$), showing that PCII with 34% and PCIII with 7.3% are far from $l = 20\% \pm 3\%$. This test is justified since in PCA all variables have (0,1) normalization, so any PC with an eigenvalue less than 1 is not worth consideration. This criterion to decide the dimensionality of the manifold on the space parameters, also called “eigenvalue one,” has gained almost universal acceptance (see Brosche 1973 and Bujarrabal et al. 1981 for the earliest papers applying the PCA technique to galaxy samples).

Since PCI and PCII contain no more than 88% of the total variance and other PCs present very small eigenvalues, we show that the addition of O/H , $W_{H\beta}$, and $[O III]/[O II]$ does not contribute to explaining the total variance of the space parameters and hence they cannot be used simultaneously to reduce the scatter in the L - σ relation. These three well-known indicators of the physical conditions in star-forming regions are strongly correlated with each other and the correlations found

Table 8
Variance Matrix: Eigenvectors and Eigenvalues

	Principal Component		
	I	II	III
$\log L_{H\alpha}$	0.39	-0.88	-0.11
$\log \sigma_H$	0.66	-0.70	-0.08
$\log (O/H)$	0.86	0.07	0.51
$\log W_{H\beta}$	-0.77	-0.54	0.25
$\log [O III]/[O II]$	-0.88	-0.38	0.16
Eigenvalues	2.69	1.70	0.37
% variance	53.9%	34.0%	7.3%

here are in good agreement with early findings (e.g., Campbell et al. 1986). The interrelationships between them are known and of intense debate in the literature (Terlevich et al. 2004; Hoyos & Díaz 2006, and references therein). This introduces a problem commonly faced by the PCA technique and multiple regression known as collinearity (or multicollinearity). Multicollinearities are often indicated by large correlations between subsets of the variables which can be seen in the correlation matrix for variables O/H , $W_{H\beta}$, and $[O III]/[O II]$ (Table 7). These three parameters are the ones that have high loadings of PCI, hence they are the variables that are most closely related to PCI (Table 8). On the other hand, the high loadings in PCII identify $L_{H\alpha}$ and σ_H as the parameters most closely related to PCII.

The main result of the above analysis is that PCI can be thought of as a measure of physical conditions in H II Gs, whereas PCII is a measure of the strength of the L - σ relation. Note that we do not invoke any prior knowledge about the physical origin of the L - σ relation. As PCs are pairwise uncorrelated, the conclusion is that physical conditions are responsible for part of the observed scatter in the L - σ relation, though the three parameters studied here cannot be used simultaneously to explain that. Note that σ_H presents its highest loading in PCII, which suggests that it is not a primary consequence of internal physical conditions (measured by these three parameters), and is possibly not controlled by subsequent mechanical feedback processes due to massive stellar evolution. However, the weaker but real correlation between σ_H and O/H ($r = 0.47$, see Table 7) is responsible for the non-negligible loading for σ_H in PCI (0.66). It shows that O/H introduces some degree of multicollinearity as an additional independent parameter in the L - σ relation. Although a high degree of multicollinearity does not violate the assumptions of the regression model, it influences the variance of the estimated regression coefficients (partial slopes and intercept). We will present the σ - Z relation in the context of the discussion about the internal dynamics of H II Gs in Section 5.1.

For now, we are not interested in fully predicting the dependent variable $L_{H\alpha}$ based on the other parameters studied here. They present a high degree of multicollinearity mainly due to the $W_{H\beta}$ - $[O III]/[O II]$ relation. Instead, we want to identify which physical condition parameter more efficiently explains the scatter as a second independent parameter in the L - σ relation. A possible way to further investigate the variance of the space parameters, overcoming the problem of multicollinearity in PCA, is by using only a subset of parameters, where the subset is chosen so that it does not contain or it is intended to minimize multicollinearities.⁸

⁷ The loadings represent correlations between the PCs and the original variables. PCs are the new set of variables uncorrelated by definition and written as linear combinations of the original variables.

⁸ Principal component regression is also a multivariate analysis appropriate for investigating problems in which multicollinearity is present (Jolliffe 2002).

Table 9

Testing the Second Parameter through Individual Principal Component Analysis—95 Objects Undistinguished by Their Emission Line Profiles

Parameter	Principal Component		
	I	II	III
$\log L_{H\alpha}$	0.88	-0.42	0.23
$\log \sigma_H$	0.96	-0.12	-0.27
$\log (O/H)$	0.61	0.79	0.09
Eigenvalues	68.5%	27.0%	4.5%
$\log L_{H\alpha}$	0.95	0.18	-0.25
$\log \sigma_H$	0.96	-0.15	0.25
$\log W_{H\beta}$	-0.03	0.99	0.08
Eigenvalues	60.8%	34.9%	4.3%
$\log L_{H\alpha}$	-0.90	-0.36	0.24
$\log \sigma_H$	-0.97	-0.03	-0.25
$\log [O III]/[O II]$	0.38	-0.92	-0.08
Eigenvalues	63.2%	32.6%	4.2%

Table 9 presents the results of the PCA table for the same sample containing 95 objects, undistinguished by their emission line profiles or $W_{H\beta}$, for the three parameter spaces: $[L_{H\alpha}, \sigma_H, O/H]$, $[L_{H\alpha}, \sigma_H, W_{H\beta}]$, and $[L_{H\alpha}, \sigma_H, [O III]/[O II]]$. The results for $[L_{H\alpha}, \sigma_H, O/H]$ show that in addition to $L_{H\alpha}$ and σ_H , O/H has a relatively high loading in the PCI (0.61), which shows its strong relevance for explaining the variance in PCI. It results from the relatively higher correlation of O/H with σ_H as mentioned above. Therefore, PCII explains only 27% of the total variance. On the other hand, the analysis with the subset $[L_{H\alpha}, \sigma_H, W_{H\beta}]$ shows that $W_{H\beta}$ is uncorrelated with σ_H and contributes efficiently to explaining 35% of the variance in PCII. The ionization ratio $[O III]/[O II]$ also presents a higher contribution to PCII than O/H.

The residual variance of 4%–5% in PCIII (Table 9) accounts for observational errors, but a fraction of it can be explained by the fact that we have analyzed a heterogeneous sample. We have not distinguished galaxies by their emission line profiles. In fact, part of the large scatter in the high L and σ regime populated mostly by I and C galaxies (see Figure 6) may not be explained at all, since single Gaussian fits seem to not represent the internal kinematics in these systems well or the resultant line widths are not well correlated with L . In addition, there must be outliers also due to photometric errors propagated to parameters that may be perturbing the PCA results. PCA is a powerful technique that can also be used to detect outliers in data sets providing robust results. In order to obtain the distance estimators presented in the next section, we have investigated and detected outliers in the context of multiple regression.

We conclude by saying that $W_{H\beta}$ as an age estimator of the starburst in HIIGs cannot be neglected in a regression model in order to obtain a distance indicator based on the L – σ relation. The ionization ratio $[O III]/[O II]$ acts in a similar way as $W_{H\beta}$ and can be explicitly considered in the absence of $W_{H\beta}$. Finally, the results shown above do not mean that O/H cannot be used as a second parameter; instead we have verified that its efficiency to reduce the scatter of the L – σ relation may be real but seems to be smaller than using $W_{H\beta}$. Additionally, O/H introduces a higher degree of collinearity due to its relationship with σ .

4.4. Empirical Relations

Primary luminosity dependence on σ has been evaluated by the L – σ relation considering only galaxies showing nearly Gaussian emission line profiles. For a given velocity dispersion

σ and metallicity (O/H), the galaxies with the largest $H\beta$ equivalent width, $W_{H\beta}$, or ionization ratio, $[O III]/[O II]$, should also present the largest Balmer luminosities, $L_{H\alpha}$. On the other hand, for a given σ and $W_{H\beta}$ or $[O III]/[O II]$, galaxies with the lowest O/H ratio should also present the largest $L_{H\alpha}$. The results found here for the L – σ relation (Table 6) and PCA (Section 4.3), as well as those in early studies (Terlevich & Melnick 1981; MTM), corroborate the same empirical model for HIIGs. Therefore, we need to obtain precise regression coefficients through multiple regressions.

Let us derive a set of empirical relations that can provide distance indicators based on the homogeneous subsample of 53 objects showing nearly Gaussian line profiles (visually classified as G) that have shown the tightest L – σ relation (Table 6). It is possible that some I or even C galaxies would fit in a regression model increasing the statistical significance of the regression coefficients, but in general, as shown in Section 3.4, they contribute to flattening the L – σ relation, increasing its scatter, especially in the regime of high L and σ values. This suggests that some of them do not share the same physical properties as most of the G galaxies or the single fit procedure to derive their resultant σ is not appropriate. These objects may also suffer differentially from aperture effects (Section 4.1). The sample containing 53 objects was chosen instead of the more restrictive one (37 objects), selected by the semi-quantitative criterion (Section 4.2), since the latter is not well represented in the range $1.6 < \log \sigma < 1.8$.

Multiple regression fits for the 53 objects are shown in Table 10. Linear fits to the L – σ relation for the same sample were also presented in Table 6. Note that the scatter given by the rms of the multiple regression fits did not significantly reduce by including a second or a third independent parameter. It is mainly due to the presence of outliers. Outliers may not introduce a significant problem in the L – σ relation (shown in Figure 7 and Table 6) because L and σ outlying measurements do not surpass the intrinsic scatter (rms ~ 0.30). We have included O/H, $W_{H\beta}$, and $[O III]/[O II]$, each carrying a potential source of error. Some data were in fact compiled from different works and they may not have been obtained at the exact same region in the galaxies. Specialized statistics used to detect outliers in the context of multiple regressions are the computations of leverage, discrepancy (studentized residual),⁹ and influence indices (Cook’s D).¹⁰ Conceptually, influence represents the product of leverage and discrepancy. These are known as the three characteristics of potentially errant data points (see Cohen et al. 2003, for a didactic presentation and concepts). Using this methodology, eight data points were deleted from the sample containing 53 objects. We have verified that the presence of these outliers is mainly due to the inclusion of objects of an uncertain nature (MRK 1201 and MRK 1318), objects with data considered from different sources (Tol 1008-286 and UM 463), and objects with unusually high uncertainties in derived parameters due to low S/N spectra (UM 417, Tol 0505-387, UM 559, and Tol 2138-397). Thus, Table 10 also shows a set of empirical relations based on a sample of 45 objects without outliers. For an rms comparison with the ones from regression models with two or three independent parameters, we also presented the linear fit OLS(Y|X) to L – σ relation for the sample containing 45 objects free from outliers. We reproduced a new version of the early

⁹ Also called “externally studentized residual” or “studentized deleted residual.”

¹⁰ DFFITS is another global measure of influence very closely related to Cook’s D .

Table 10
Multiple Regressions for $L_{H\alpha}$, σ_H , O/H, $W_{H\beta}$, and [O III]/[O II]

Parameters	Regressions for $\log L_{H\alpha}$	rms
Galaxies with Gaussian profiles (53 objects) ^a		
$L-\sigma$	$(35.29 \pm 0.42) + (3.72 \pm 0.31)\log \sigma$	0.312
$L-\sigma-O/H$	$(38.22 \pm 1.02) + (4.19 \pm 0.31)\log \sigma - (0.44 \pm 0.14)\log(O/H)$	0.289
$L-\sigma-W_{H\beta}$	$(34.60 \pm 0.39) + (3.84 \pm 0.25)\log \sigma + (0.32 \pm 0.08)\log W_{H\beta}$	0.274
$L-\sigma-[O III]/[O II]$	$(34.69 \pm 0.38) + (4.06 \pm 0.27)\log \sigma + (0.34 \pm 0.09)\log [O III]/[O II]$	0.275
$L-\sigma-O/H-W_{H\beta}$	$(35.63 \pm 1.43) + (3.96 \pm 0.31)\log \sigma - (0.14 \pm 0.18)\log(O/H) + (0.27 \pm 0.11)\log W_{H\beta}$	0.275
$L-\sigma-O/H-[O III]/[O II]$	$(35.95 \pm 1.01) + (4.17 \pm 0.22)\log \sigma - (0.17 \pm 0.17)\log(O/H) + (0.27 \pm 0.11)\log [O III]/[O II]$	0.275
Parameters	Regressions for $\log L_{H\alpha}$	rms
Galaxies with Gaussian profiles (45 objects) without outliers		
$L-\sigma$	$(35.26 \pm 0.38) + (3.76 \pm 0.27)\log \sigma$	0.270
$L-\sigma-O/H$	$(39.94 \pm 0.99) + (4.33 \pm 0.25)\log \sigma - (0.68 \pm 0.14)\log(O/H)$	0.217
$L-\sigma-W_{H\beta}$	$(34.58 \pm 0.30) + (3.78 \pm 0.20)\log \sigma + (0.39 \pm 0.06)\log W_{H\beta}$	0.201
$L-\sigma-[O III]/[O II]$	$(34.64 \pm 0.30) + (4.09 \pm 0.21)\log \sigma + (0.39 \pm 0.07)\log [O III]/[O II]$	0.204
$L-\sigma-O/H-W_{H\beta}$	$(36.64 \pm 1.38) + (4.01 \pm 0.25)\log \sigma - (0.27 \pm 0.18)\log(O/H) + (0.29 \pm 0.09)\log W_{H\beta}$	0.197
$L-\sigma-O/H-[O III]/[O II]$	$(37.04 \pm 1.29) + (4.26 \pm 0.22)\log \sigma - (0.32 \pm 0.17)\log(O/H) + (0.28 \pm 0.09)\log [O III]/[O II]$	0.198

Note. ^a The same subsample with 53 G objects used in Table 6.

empirical model $L-\sigma-O/H$ used by MTM to derive their distance indicator with the same rms scatter of $\delta \log L_{H\alpha} = 0.22$. Independent functional forms for $L-\sigma-W_{H\beta}$ and $L-\sigma-[O III]/[O II]$ produce virtually the same result and they are both more efficient than O/H as a second independent parameter in the $L-\sigma$ relation reducing the rms scatter to $\delta \log L_{H\alpha} = 0.20$. In addition, we present the “true” empirical model for HII Gs, $L-\sigma-O/H-W_{H\beta}$ (R1), and $L-\sigma-O/H-[O III]/[O II]$ (R2). The scatter has not been significantly reduced by the inclusion of a third independent parameter—O/H in $L-\sigma-W_{H\beta} \sim 2\%$ and O/H in $L-\sigma-[O III]/[O II] \sim 3\%$ —but the residual is compatible with the expected error in luminosity, which prevents us from determining what fraction is intrinsic.

It is an important result that $W_{H\beta}$ alone can account for a significant fraction of the scatter in the $L-\sigma$ relation ($\sim 25\%$) with a minimum degree of collinearity. $W_{H\beta}$ has the advantage of being a simpler parameter to obtain from the spectra, though it depends on continuum detection. Alternatively, if the intense [O III] $\lambda\lambda 4959, 5007$ and [O II] $\lambda 3727$ lines are detected, one can use the $L-\sigma-[O III]/[O II]$ regression model with the same precision. On the other hand, the $L-\sigma-O/H$ empirical model as distance indicator would be more difficult to apply at great distances since it requires the detection of the [O III] $\lambda 4363$ auroral line to precisely calculate oxygen abundances by the T_e -method.

Figure 10 presents all five regression models, including those with two (panels a, b, and c) and three (panels d and e) independent parameters plotted against the observed $L_{H\alpha}$. The outliers are plotted as open red circles in all panels. Their predicted luminosity values were computed from the respective regression models for 45 objects presented in Table 10. Figure 11 presents the histograms of all five parameters used in regression models, $L_{H\alpha}$ (a), σ_H (b), O/H (c), $W_{H\beta}$ (d), and [O III]/[O II] (e), with their mean values and standard deviation in logarithmic units. These histograms characterize our calibration sample. Note that we have included some galaxies with $W_{H\beta} < 30 \text{ \AA}$ in our sample, which were not included by MTM in their calibration sample. Our calibration sample with 45 local objects is a good representative sample of HII Gs in general. The mean, standard deviation, and median (8.03) of the distribution of metallicity (Figure 11, panel c) are consistent with studies that characterize the population of HII Gs from much larger samples (Kniazhev et al. 2004).

5. DISCUSSION

5.1. Internal Dynamics

The existence of the $L-\sigma$ relation for GHII Rs and HII Gs poses an intriguing question about the origin of the supersonic velocity widths of the emission line profiles. Several works have tried to answer this question through different approaches, but the hypothesis that these systems are gravitationally bound at least in the early stages of their evolution persists as a paradigm (Terlevich & Melnick 1981). Figure 12 presents the $\sigma-Z$ relation for the whole sample presented in PCA (Section 4.3, 95 objects) and for those galaxies presented in the calibration sample (Section 4.4, 45 objects). If σ correlates with metallicity in a similar manner as in gravitationally bound systems, the underlying relation could be the one between mass and metallicity. We present the bisector regression fits for different samples in the caption of Figure 12. In a recent work considering a large sample of HII Gs, Salzer et al. (2005) have shown the existence of the $L-Z$ relation for these systems. The near-infrared (NIR) $L^{0.20} \propto Z$ relation found by the authors, which more directly reflects the underlying relationship between mass and metallicity, could be compared with our results in order to check whether the gravitational interpretation of the $L-\sigma$ relation of HII Gs is acceptable. However, the NIR luminosity comes mostly from the old stellar population, which may not be directly associated with the current mass of the starburst. Another option would be to compare the B -band $L-Z$ with our $Z-\sigma$ relation. In fact, if we use the scaling relation $L^{0.28} \propto Z$ derived for the B band by Salzer et al. (2005) and consider the $Z \propto \sigma^{1.6}$ found here, we get closer to the $L \propto \sigma^4$. It still cannot constrain much about the gravitational interpretation since we have to explain how σ of gas from the current starburst correlates with metallicity. A simple explanation would be that metal-rich galaxies produce more massive starbursts, and this should be verified with observations. These interesting questions are beyond the scope of this work and should be further investigated.

Another hint about the origin of velocity widths found in HII Gs is provided by the systematic difference found between the width of HII and [O III] lines. This difference was first found in GHII Rs by Hippelein (1986). Figure 13 shows the differences found for our sample of HII Gs. In the left panel of Figure 13, we plot all galaxies with two lines observed,

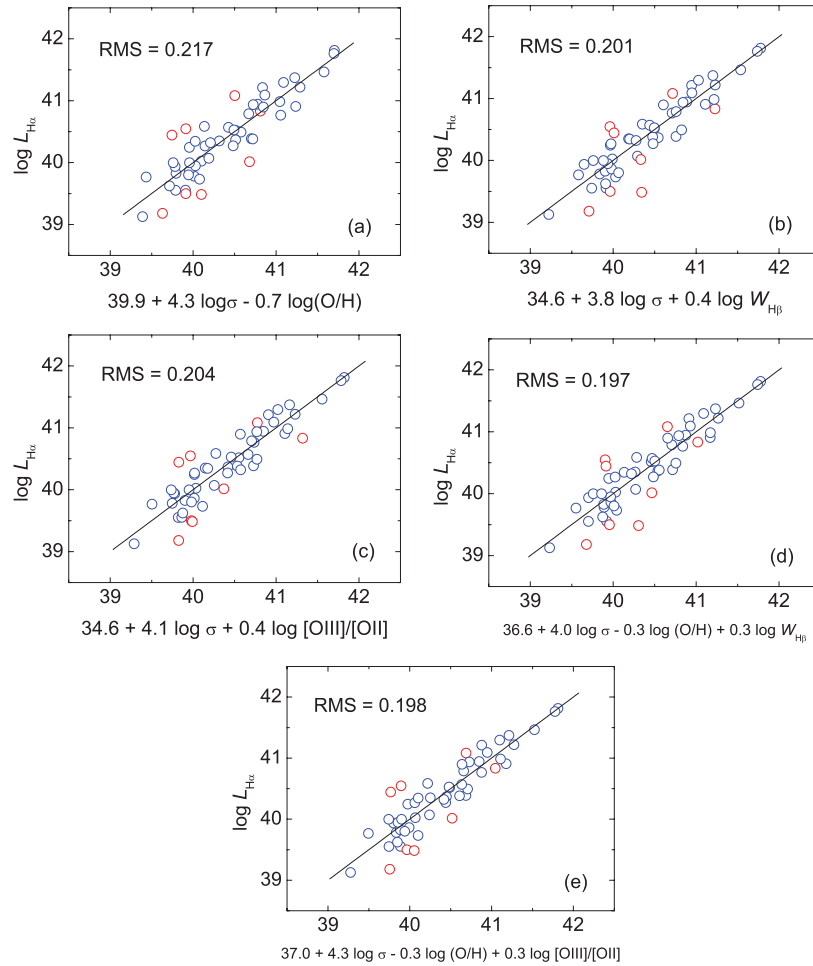


Figure 10. Regression models plotted against observed H α luminosities for 53 objects. The functional forms are presented in the x axis of each graph. The solid lines represent the 1 to 1 lines fitted to the data. The calibration galaxies are plotted as open blue circles, whereas the outliers are plotted as open red circles.

(A color version of this figure is available in the online journal.)

H β and [O III] 4959 Å, whereas in the right panel we plot only the lines with the highest S/N with the smallest σ errors ($\delta\sigma < 1.2 \text{ km s}^{-1}$). We do not see any systematic difference between these measurements above $\sim 50 \text{ km s}^{-1}$. In fact, we note high discrepancies ($5\text{--}20 \text{ km s}^{-1}$) between σ_{H} and $\sigma_{[\text{O III}]}$ with no trend. On the other hand, we see that HII regions showing σ values in the regime $15 \text{ km s}^{-1} < \sigma < 50 \text{ km s}^{-1}$ present the intrinsic kinematic property also found in GHII regions. There is a small systematic difference between σ derived from both ions, $\langle \sigma_{\text{H}} - \sigma_{[\text{O III}]} \rangle = 1\text{--}2 \text{ km s}^{-1}$. It seems to be a special consequence of coupled kinematic and physical conditions in these systems. A possible explanation would be the existence of a well-behaved ionization structure, in which more excited ions are concentrated closer to the ionizing sources and densest regions. However, a gradient of velocity dispersion is not observed at scales of tens to hundreds of parsecs in giant HII regions. Other kinematic mechanisms that can be invoked to account for the observed systematic difference can be associated with turbulence (Hippelstein 1986).

We note that many HII regions presented in Figure 13 (right panel) are in fact those classified as Gaussian line profiles (open circles). This is another indication that these systems define a homogeneous sample in terms of their internal kinematics. Although our sample presents few galaxies with both measurements in the high σ regime, Figure 13 (left panel) suggests that

HII regions with $\sigma > 60 \text{ km s}^{-1}$ do not seem to share the same kinematic properties as those with $\sigma < 60 \text{ km s}^{-1}$.

5.2. Age Effects: Short- and Long-term Evolution

We have shown that the age effect (short-term evolution) is the first-order effect over the $L\text{--}\sigma$ relation and should not be neglected explicitly in an empirical relation in order to derive a distance indicator. Here we have tested $W_{\text{H}\beta}$ and [O III]/[O II] as fiducial chronometers of the starburst. Both are virtually equally efficient in explaining the scatter in the $L\text{--}\sigma$ plane. In order to reduce the scatter due to an age effect, one does not need a parameter that measures the burst age, but one that efficiently measures the luminosity variation of the starburst as it ages. Photoionized models have shown that the most robust parameter for measuring the luminosity evolution of the starburst is in fact $W_{\text{H}\beta}$ (Stasińska & Leitherer 1996; Martín-Manjón et al. 2008). Its advantage is due to its weak dependence on metallicity; [O III]/[O II] and $W_{[\text{O III}]5007}$ are more sensitive to metallicity. Figure 14 shows the predictions from photoionized models by Stasińska & Leitherer (1996) for H β luminosity evolution of the starburst as a function of $W_{\text{H}\beta}$ (panels b and d) and [O III]/[O II] (panels a and c), for a given starburst mass of $10^6 M_{\odot}$ and two metallicities $12 + \log(\text{O}/\text{H}) = 7.93$ (panels a and b) and 8.33 (c and d). It is possible to see that $L(W_{\text{H}\beta})$ presents a nearly constant curve shape in both abundance sets, whereas $L([\text{O III}]/$

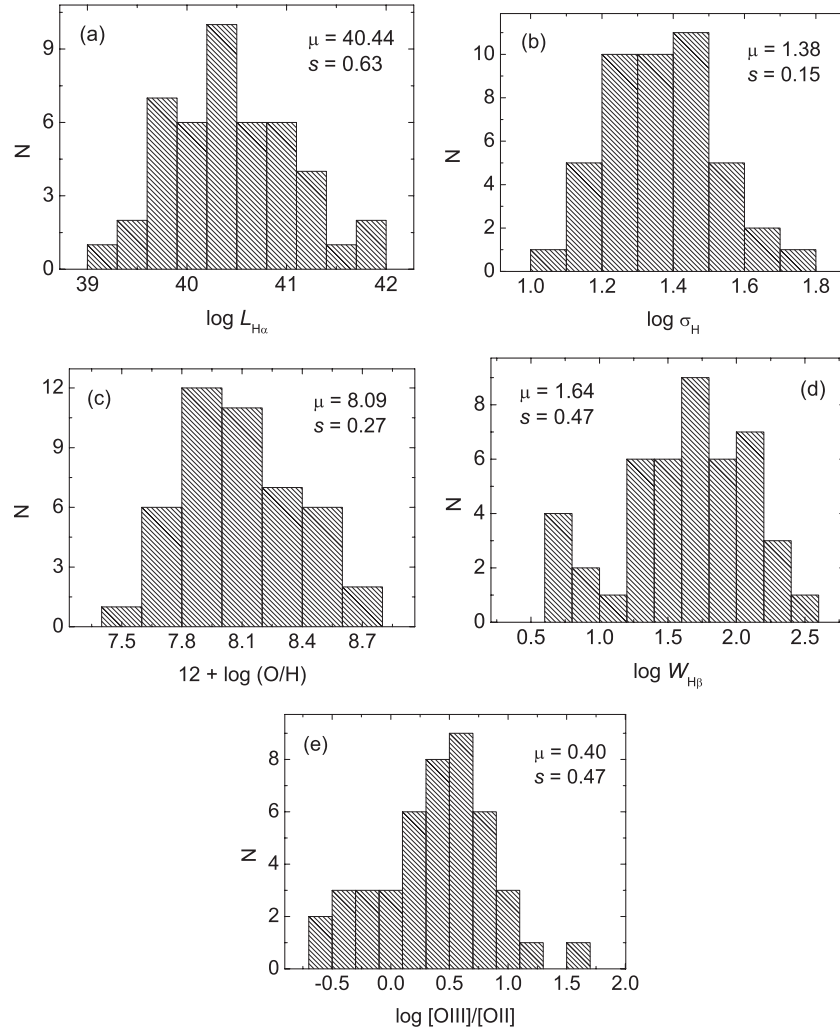


Figure 11. Histograms for all parameters in the calibration sample (45 objects) in logarithmic units. Means (μ) and standard deviations (s) of the distributions are shown in each plot.

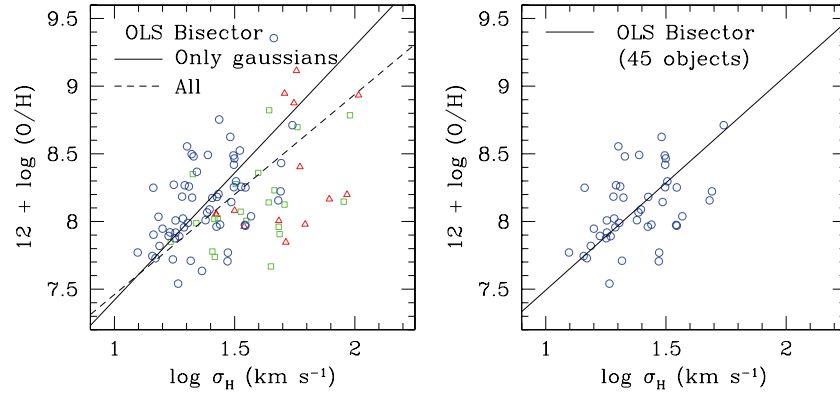


Figure 12. Left panel: the σ - Z relation presented by 95 objects included in PCA. The solid and dashed lines represent the OLS bisector fits to the entire sample, $12 + \log(\text{O}/\text{H}) = (5.98 \pm 0.19) + (1.48 \pm 0.14) \log \sigma_{\text{H}}$, and to the G sample, $12 + \log(\text{O}/\text{H}) = (5.54 \pm 0.34) + (1.88 \pm 0.26) \log \sigma_{\text{H}}$, 60 objects, respectively. Right panel: the σ - Z relation for the 45 objects used in the calibration sample without outliers (Table 10). The solid line represents the OLS bisector fit, $12 + \log(\text{O}/\text{H}) = (5.91 \pm 0.23) + (1.59 \pm 0.17) \log \sigma_{\text{H}}$.

(A color version of this figure is available in the online journal.)

[O II]) does not present a monotonic curve in the $12 + \log(\text{O}/\text{H}) = 8.33$ set, especially in the first 5 Myr of the starburst. Note that $L(W_{\text{H}\beta})$ still presents a more stable curve for $\log W_{\text{H}\beta} > 1.5$ or $\sim 30 \text{ \AA}$. Models considering the continuous burst scenario have shown that $W_{\text{H}\beta}$ is in fact a robust age indicator of the

starburst even for a significant presence of an underlying stellar population (Martín-Manjón et al. 2008).

Metallicity itself is also a tracer of evolution, though it is more closely linked to the long-term history of the star formation of the galaxy. The metallicity given by the O/H ratio, as proposed

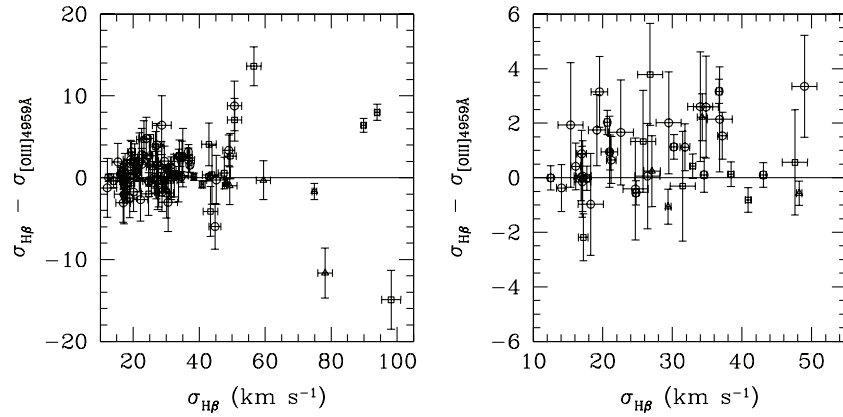


Figure 13. Comparison between σ derived from $H\beta$ and $[O III]\lambda 4959$. Left panel: all galaxies included. Right panel: only galaxies presenting $\delta\sigma < 2 \text{ km s}^{-1}$. A small systematic difference $\sigma_H - \sigma_{[O III]} = 1\text{--}2 \text{ km s}^{-1}$ is verified for galaxies with $\sigma \lesssim 60 \text{ km s}^{-1}$.

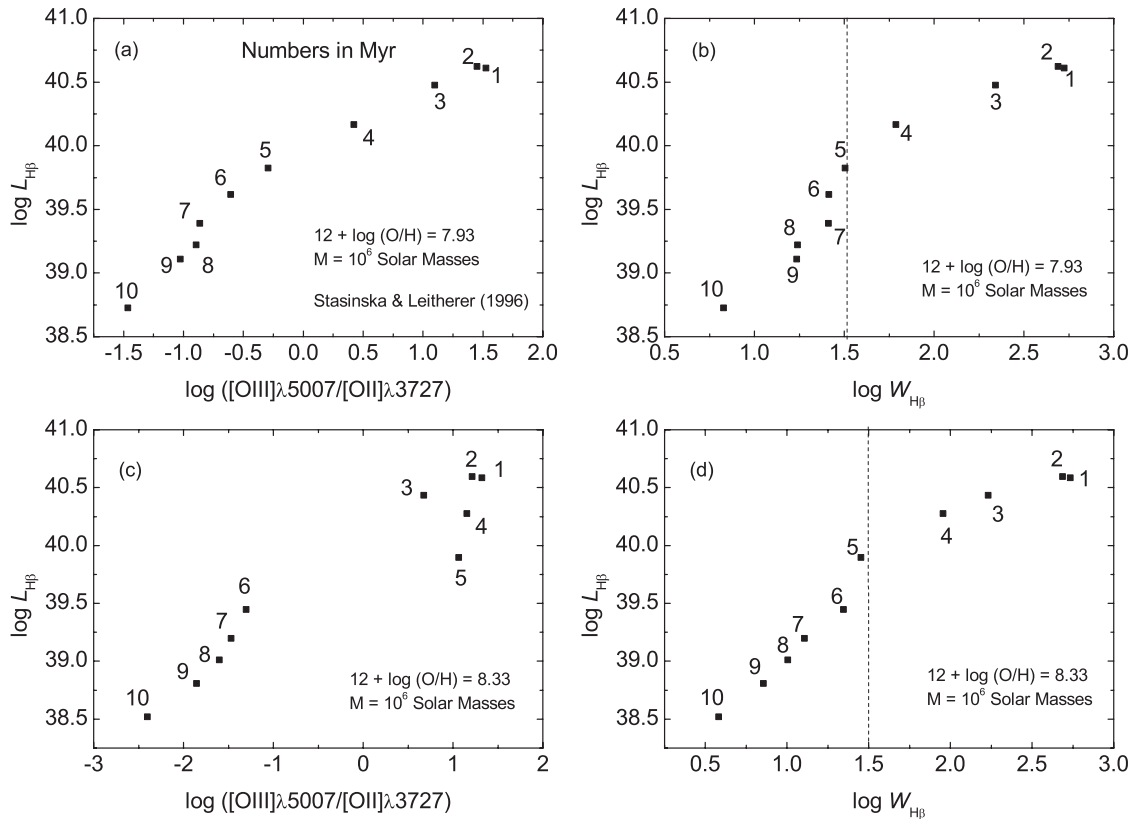


Figure 14. $H\beta$ luminosity as a function of $[O III]\lambda 5007/[O II]\lambda 3727$ (a and c) and $H\beta$ equivalent width (b and d) in logarithmic units as predicted by single stellar population models by Stasińska & Leitherer (1996) with $M = 10^6 M_{\odot}$ and two metallicities, $12 + \log (O/H) = 7.93$ (a and b) and 8.33 (c and d). Numbers indicate the age of the starburst in Myr. Vertical dotted lines in panels b and d indicate the cutoff value $W_{H\beta} \sim 30 \text{ \AA}$ which coincides with age $\sim 5 \text{ Myr}$ of the starburst in both models.

by MTM, may represent a second parameter in the L – σ relation, since successive chemical enrichment promoted by generations of stars may globally affect the luminosity evolution (short term) of each starburst.

Recent efforts have been made by Plionis et al. (2010) to investigate the precision required for distance determinations of high- z HII Gs to achieve cosmological goals. Following Melnick et al. (2000), these authors propose applying scaling relations, like the ones derived here, to measure the dark energy equation of state, $w(z)$, and the matter content of the universe Ω_m , by using the Hubble diagram for HII Gs as an alternative to SNIa above $z \sim 1$. Considerations made here about the systematic effects of the L – σ relation may be valuable for its further application.

6. SUMMARY

We have presented a new large data set of line width measurements for star-forming regions in over 100 HII Gs. This was used to analyze in some detail the line profile class as a function of the galaxy morphology, line-fitting methodologies, PCA of the observed physical parameters, and the statistical methods of data selection, rejection, and linear regression to reach our final conclusions on the calibration of the L – σ relation for local HII Gs.

1. The family of HII Gs as first cataloged mainly by emission line detection does not represent a homogeneous sample in terms of their internal kinematics. Gaussianity of their

emission line profiles is closely related to the physical origin of the L – σ relation since galaxies showing the most Gaussian line profiles seem to produce a steeper $L \propto \sigma^4$ relation with the least scatter ($\delta \log L_{H\alpha} = 0.30$). These objects represent a more homogeneous class in terms of kinematics and define the key property of the HII G targets of the L – σ relation. These objects also seem to suffer less from aperture effects.

2. The L – σ relation is simultaneously affected by the short- and the long-term evolution of the starburst. Both effects can be accounted for to predict Balmer luminosity in a functional form in order to obtain a more accurate distance indicator. Here we have quantified the contribution of H β equivalent width and the ionization parameter [O III] $\lambda\lambda 5007, 4959$ /[O II] $\lambda 3727$ as measures of short-term evolution and O/H as a measure of the long-term evolution.
3. We calibrated the L – σ –O/H empirical relation, previously presented by MTM, as the distance indicator of the HII Gs and provided an alternative set of new empirical relations, especially the L – σ – $W_{H\beta}$ relation, that can be used with greater accuracy ($\delta \log L_{H\alpha} = 0.20$ or 0.5 mag) and simplicity to determine distances of HII Gs at high redshifts with application to cosmology questions.

V.B. acknowledges his CAPES scholarship. We are grateful to the staff at ESO who have helped us with the many observing runs at La Silla. We are very thankful to Roberto Terlevich, Elena Terlevich, Guillermo Tenorio-Tagle, and Casiana Muñoz-Tuñón for numerous discussions on topics related to this work over the years. Finally, we are thankful to the anonymous referee for his/her comments which improved the paper.

REFERENCES

- Arsenault, R., & Roy, J.-R. 1988, *A&A*, **201**, 199
- Bordalo, V., Plana, H., & Telles, E. 2009, *ApJ*, **696**, 1668
- Bosch, G., Terlevich, E., & Terlevich, R. 2002, *MNRAS*, **329**, 481
- Brosche, P. 1973, *A&A*, **23**, 259
- Bujarrabal, V., Guibert, J., & Balkowski, C. 1981, *A&A*, **104**, 1
- Campbell, A., Terlevich, R., & Melnick, J. 1986, *MNRAS*, **223**, 811
- Chu, Y.-H., & Kennicutt, R. C., Jr. 1994, *ApJ*, **425**, 720
- Cohen, J., Cohen, P., West, S. G., & Aiken, L. S. 2003, *Applied Multiple Regression/Correlation Analysis for the Behavioral Sciences* (3rd ed.; Mahwah, NJ: L. Erlbaum Associates)
- Coziol, R., Demers, S., Pena, M., Torres-Peimbert, S., Fontaine, G., Wesemael, F., & Lamontagne, R. 1993, *AJ*, **105**, 35
- Denicoló, G., Terlevich, R., & Terlevich, E. 2002, *MNRAS*, **330**, 69
- Erb, D. K., Steidel, C. C., Shapley, A. E., Pettini, M., & Adelberger, K. L. 2004, *ApJ*, **612**, 122
- Fairall, A. P. 1980, *MNRAS*, **191**, 391
- Fernández Lorenzo, M., Cepa, J., Bongiovanni, A., Pérez García, A. M., Ederoclite, A., Lara-López, M. A., Pović, M., & Sánchez-Portal, M. 2011, *A&A*, **526**, A72
- Fernández Lorenzo, M., Cepa, J., Bongiovanni, A., Pérez García, A. M., Lara-López, M. A., Pović, M., & Sánchez-Portal, M. 2010, *A&A*, **521**, A27
- François, P. 1999, *Fiber Extended Range Optical Spectrograph User's Manual*
- Fuentes-Masip, O., Muñoz-Tuñón, C., Castañeda, H. O., & Tenorio-Tagle, G. 2000, *AJ*, **120**, 752
- García-Díaz, M. T., Henney, W. J., López, J. A., & Doi, T. 2008, *RevMexAA*, **44**, 181
- Hippenle, H. H. 1986, *A&A*, **160**, 374
- Hoyos, C., & Díaz, A. I. 2006, *MNRAS*, **365**, 454
- Isobe, T., Feigelson, E. D., Akritas, M. G., & Babu, G. J. 1990, *ApJ*, **364**, 104
- Izotov, Y. I., Chaffee, F. H., & Green, R. F. 2001, *ApJ*, **562**, 727
- Izotov, Y. I., & Thuan, T. X. 1998, *ApJ*, **500**, 188
- Jolliffe, I. T. 2002, *Principle Component Analysis* (2nd ed.; Berlin: Springer)
- Kehrig, C., Telles, E., & Cuisinier, F. 2004, *AJ*, **128**, 1141
- Kehrig, C., Vilchez, J. M., Sánchez, S. F., Telles, E., Pérez-Montero, E., & Martín-Gordón, D. 2008, *A&A*, **477**, 813
- Kewley, L. J., Jansen, R. A., & Geller, M. J. 2005, *PASP*, **117**, 227
- Kniazev, A. Y., Pustilnik, S. A., Grebel, E. K., Lee, H., & Pramskij, A. G. 2004, *ApJS*, **153**, 429
- Kniazev, A. Y., Pustilnik, S. A., Ugryumov, A. V., & Pramsky, A. G. 2001, *A&A*, **371**, 404
- Kunth, D., Sargent, W. L. W., & Kowal, C. 1981, *A&AS*, **44**, 229
- Lagos, P., Telles, E., & Melnick, J. 2007, *A&A*, **476**, 89
- Law, D. R., Steidel, C. C., Erb, D. K., Larkin, J. E., Pettini, M., Shapley, A. E., & Wright, S. A. 2009, *ApJ*, **697**, 2057
- Lequeux, J., Peimbert, M., Rayo, J. F., Serrano, A., & Torres-Peimbert, S. 1979, *A&A*, **80**, 155
- Lowenthal, J. D., Koo, D. C., Simard, L., & van Kampen, E. 2009, *ApJ*, **703**, 198
- MacAlpine, G. M., Smith, S. B., & Lewis, D. W. 1977, *ApJS*, **34**, 95
- Maíz-Apellániz, J., Muñoz-Tuñón, C., Tenorio-Tagle, G., & Mas-Hesse, J. M. 1999, *A&A*, **343**, 64
- Markarian, B. E. 1967, *Astrofizika*, **3**, 55
- Martínez-Delgado, I., Tenorio-Tagle, G., Muñoz-Tuñón, C., Moiseev, A. V., & Cairós, L. M. 2007, *AJ*, **133**, 2892
- Martín-Manjón, M. L., Mollá, M., Díaz, A. I., & Terlevich, R. 2008, *MNRAS*, **385**, 854
- Masegosa, J., Moles, M., & Campos-Aguilar, A. 1994, *ApJ*, **420**, 576
- Mas-Hesse, J. M., & Kunth, D. 1999, *A&A*, **349**, 765
- Maza, J., Ruiz, M. T., Gonzalez, L. E., Wischnjowsky, M., & Pena, M. 1991, *A&AS*, **89**, 389
- Melnick, J. 1977, *ApJ*, **213**, 15
- Melnick, J. 1978, *A&A*, **70**, 157
- Melnick, J. 1979, *ApJ*, **228**, 112
- Melnick, J. 2003, in *ASP Conf. Ser. 297, Star Formation Through Time*, ed. E. Perez, R. M. Gonzalez Delgado, & G. Tenorio-Tagle (San Francisco, CA: ASP), **3**
- Melnick, J., Moles, M., Terlevich, R., & Garcia-Pelayo, J.-M. 1987, *MNRAS*, **226**, 849
- Melnick, J., Tenorio-Tagle, G., & Terlevich, R. 1999, *MNRAS*, **302**, 677
- Melnick, J., Terlevich, R., & Moles, M. 1988, *MNRAS*, **235**, 297
- Melnick, J., Terlevich, R., & Terlevich, E. 2000, *MNRAS*, **311**, 629
- Miesch, M. S., Scalo, J., & Bally, J. 1999, *ApJ*, **524**, 895
- Moiseev, A. V., Pustilnik, S. A., & Kniazev, A. Y. 2010, *MNRAS*, **405**, 2453
- Osterbrock, D. E. 1989, *Sky & Tel.*, **78**, 491
- Pagel, B. E. J., Simonson, E. A., Terlevich, R. J., & Edmunds, M. G. 1992, *MNRAS*, **255**, 325
- Papaderos, P., Guseva, N. G., Izotov, Y. I., Noeske, K. G., Thuan, T. X., & Fricke, K. J. 2006, *A&A*, **457**, 45
- Pena, M., Ruiz, M. T., & Maza, J. 1991, *A&A*, **251**, 417
- Pettini, M., Shapley, A. E., Steidel, C. C., Cuby, J.-G., Dickinson, M., Moorwood, A. F. M., Adelberger, K. L., & Giavalisco, M. 2001, *ApJ*, **554**, 981
- Pilyugin, L. S. 2000, *A&A*, **362**, 325
- Plionis, M., Terlevich, R., Basilakos, S., Bresolin, F., Terlevich, E., Melnick, J., & Chavez, R. 2010, *J. Phys.: Conf. Ser.*, **222**, 012025
- Plionis, M., Terlevich, R., Basilakos, S., Bresolin, F., Terlevich, E., Melnick, J., & Georgantopoulos, I. 2009, *J. Phys.: Conf. Ser.*, **189**, 012032
- Pustilnik, S. A., Kniazev, A. Y., Masegosa, J., Márquez, I. M., Pramskij, A. G., & Ugryumov, A. V. 2002, *A&A*, **389**, 779
- Relaño, M., Beckman, J. E., Zurita, A., Rozas, M., & Giammanco, C. 2005, *A&A*, **431**, 235
- Riess, A. G., et al. 2007, *ApJ*, **659**, 98
- Riffel, R. A. 2010, *Ap&SS*, **327**, 239
- Rozas, M., Richer, M. G., López, J. A., Relaño, M., & Beckman, J. E. 2006, *A&A*, **455**, 539
- Salzer, J. J. 1989, *ApJ*, **347**, 152
- Salzer, J. J., Lee, J. C., Melbourne, J., Hinz, J. L., Alonso-Herrero, A., & Jangren, A. 2005, *ApJ*, **624**, 661
- Scalo, J., & Chappell, D. 1999, *MNRAS*, **310**, 1
- Shaw, R. A., & Dufour, R. J. 1995, *PASP*, **107**, 896
- Siegel, E. R., Guzmán, R., Gallego, J. P., Orduña López, M., & Rodríguez Hidalgo, P. 2005, *MNRAS*, **356**, 1117
- Smith, M. G., Aguirre, C., & Zelman, M. 1976, *ApJS*, **32**, 217
- Stasińska, G., & Izotov, Y. 2003, *A&A*, **397**, 71
- Stasińska, G., & Leitherer, C. 1996, *ApJS*, **107**, 661
- Surace, C., & Comte, G. 1998, *A&AS*, **133**, 171
- Telles, E., Melnick, J., & Terlevich, R. 1997, *MNRAS*, **288**, 78

- Telles, E., Muñoz-Tuñón, C., & Tenorio-Tagle, G. 2001, [ApJ](#), **548**, 671
- Telles, E., & Terlevich, R. 1993, [Ap&SS](#), **205**, 49
- Tenorio-Tagle, G., Munoz-Tunon, C., & Cox, D. P. 1993, [ApJ](#), **418**, 767
- Tenorio-Tagle, G., Muñoz-Tuñón, C., Pérez, E., Silich, S., & Telles, E. 2006, [ApJ](#), **643**, 186
- Terlevich, R., & Melnick, J. 1981, *MNRAS*, **195**, 839
- Terlevich, R., Melnick, J., Masegosa, J., Moles, M., & Copetti, M. V. F. 1991, *A&AS*, **91**, 285
- Terlevich, R., Silich, S., Rosa-González, D., & Terlevich, E. 2004, *MNRAS*, **348**, 1191
- van Zee, L., Salzer, J. J., Haynes, M. P., O'Donoghue, A. A., & Balonek, T. J. 1998, [AJ](#), **116**, 2805
- Vílchez, J. M., & Iglesias-Páramo, J. 2003, [ApJS](#), **145**, 225
- Whitford, A. E. 1958, [AJ](#), **63**, 201
- Zwicky, F., Herzog, E., & Wild, P. (ed.) 1966, *Catalogue of Galaxies and of Clusters of Galaxies*, Vol. 3 (Pasadena, CA: California Institute of Technology)